

"Made available under NASA sponsorship
in the interest of early and wide dis-
semination of Earth Resources Survey
Program information, and without liability
for any use made thereof."

TRW

E7.4-10401

CR-137225

(E74-10401) EVALUATION OF DIGITAL
CORRECTION TECHNIQUES FOR ERTS IMAGES
Final Report and Semiannual Progress
Report (TRW Systems Group) 80 p HC
\$7.00

N74-19009

Unclas

CSCI 05E G3/13 00401



Order in graphy day here
ERO Data Center
10th and Dakota Avenue
Sioux Falls, SD 57198

TRW
SYSTEMS GROUP

One Space Park • Redondo Beach, California 90278

EVALUATION OF DIGITAL CORRECTION TECHNIQUES FOR ERTS IMAGES

S.S. RIFMAN
D.M. McKINNON

TRW SYSTEMS GROUP
ONE SPACE PARK
REDONDO BEACH, CA 90278

MARCH 1974
FINAL REPORT

DO NOT REPRODUCE

Original photography may be purchased from
EROS Data Center
10th and Dakota Avenue
Sioux Falls, SD 57198

PREPARED UNDER NASA CONTRACT NAS5-21814 FOR
GODDARD SPACE FLIGHT CENTER
Greenbelt, Maryland 20771

1. Report No. 20634-6003-TU-00		2. Government Accession No.		3. Recipient's Catalog No.	
4. Title and Subtitle Evaluation of Digital Correction Techniques for ERTS Images - Final Report				5. Report Date March, 1974	
				6. Performing Organization Code	
7. Author(s) S.S. Rifman D.M. McKinnon				8. Performing Organization Report No.	
9. Performing Organization Name and Address TRW Systems Group One Space Park Redondo Beach, Cal. 90278				10. Work Unit No.	
				11. Contract or Grant No. NAS5-21814	
12. Sponsoring Agency Name and Address NASA Goddard Space Flight Center Greenbelt, Maryland 20771 Technical Officer: Frederick Gordon, Jr.				13. Type of Report and Period Covered Final Report Aug., '72-Feb., '73	
				14. Sponsoring Agency Code	
15. Supplementary Notes					
16. Abstract Bulk computer compatible tape data for ERTS Multispectral Scanner and Return Beam Vidicon data have been processed by all digital methods. This document contains a summary of all results obtained in the course of this study contract, including: Automatic Ground Control Point Extraction, Automatic Reseau Extraction, Kalman Filter Attitude Refinement, Piecewise Low-Order Distortion Model, and resampling by means of Nearest-Neighbor, Bilinear and the TRW Cubic Convolution Process. High accuracies and throughput have been demonstrated for each of the processes evaluated.					
17. Key Words (Selected by Author(s)) Digital Processing ERTS Imagery Image Resampling Interpolation CPU Time				18. Distribution Statement	
19. Security Classif. (of this report) U		20. Security Classif. (of this page) U		21. No. of Pages 79	
				22. Price*	

*For sale by the Clearinghouse for Federal Scientific and Technical Information, Springfield, Virginia 22151.

TABLE OF CONTENTS

	<u>Page</u>
1. INTRODUCTION AND SUMMARY	1-1
1.1 STUDY SCOPE	1-1
1.2 STUDY APPROACH	1-3
1.3 SUMMARY OF MAJOR RESULTS	1-4
1.4 CONCLUSIONS AND RECOMMENDATIONS	1-9
1.5 PUBLISHED PAPERS	1-0
1.6 NEW TECHNOLOGY	1-9
2. MSS DATA PROCESSING	2-1
2.1 INTRODUCTION	2-1
2.2 METHODOLOGY	2-3
2.3 MSS DATA PROCESSING RESULTS	2-5
2.3.1 GCP Extraction Precision	2-5
2.3.2 Kalman Filter Performance	2-8
2.3.3 Pseudo-Reseau Grid Modeling Errors	2-15
2.3.4 Pass I Precision	2-22
2.3.5 Processed Imagery	2-23
2.3.6 Throughput	2-29
3. RBV DATA PROCESSING	3-1
3.1 INTRODUCTION	3-1
3.2 APPROACH	3-3
3.2.1 Reseau Extraction	3-3
3.2.2 Ground Truth Computation for Attitude and Ephemeris Error	3-6
3.2.3 Pseudo-Reseau Grid Generation	3-8
3.2.4 Bilinear Coefficient	3-12
3.3 RBV DATA PROCESSING RESULTS	3-13
4. RESAMPLING COMPARISONS	4-1
5. REFERENCES	5-1

()
PRECEDING PAGE BLANK NOT FILMED

LIST OF ILLUSTRATIONS

	<u>Page</u>
1.1 Study Schedule	1-5
1.2 Top Level Function Flow for ERTS Data Processing	1-6
2.1 MSS Subsystem	2-2
2.2 MSS Program Functional Schematic	2-4
2.3 GCP Window Extraction from a Search Neighborhood	2-6
2.4 Polynomial Models of Roll Time-Series	2-11
2.5 Polynomial Models of Pitch Time-Series	2-12
2.6 Polynomial Models of Yaw Time-Series	2-13
2.7 Norm of GCP Residual Error vs GCP Observation Number	2-14
2.8 Attitude Estimation Uncertainty	2-16
2.9 Statistics Based on a Sample of 10 GCP's	2-17
2.10 Mean Absolute and Maximum Random Position Errors	2-21
2.11 Bulk Image 1062-15190-5 from CCT Data	2-24
2.12 NASA Precision Product for Image 1062-15190-5	2-25
2.13 Detail of TRW Precision Product for Image 1062-15190-5...	2-26
2.14 Detail of TRW Precision Product for Image 1062-15190-7...	2-27
2.15 Detail from NASA Precision Product for Image 1062-15190-7	2-28
3.1 RBV Subsystem	3-2
3.2 The Statistical Function (σ/σ_R) for the Piecewise Biquadratic Approach	3-10
3.3 Reseau Subregions	3-11
3.4 System Corrected RBV Scene 1002-18134-1	3-15
3.5 Detail From Scene 1002-18134-1 Bulk Data	3-16
3.6 Detail from TRW Precision Product for Scene 1002-18134-1.	3-17
3.7 Detail for NASA System Corrected Product for Scene 1002-18134-1	3-18
4.1 Three Interpolation Kernels	4-3
4.2 Nearest-Neighbor and Bilinear Interpolation	4-4

LIST OF ILLUSTRATIONS (Continued)

	<u>Page</u>
4.3 Resampling Errors	4-5
4.4 Corrected Image Detail for Three Interpolation Algorithms	4-7
4.5 Nearest-Neighbor Processed Image Detail	4-8
4.6 TRW Cubic Convolution Processed Image Detail	4-9
4.7 Detail of Precision Processed Scene 1062-15190-5	4-10
4.8 Power Spectral Density, Averaged for 100 Lines	4-11
4.9 Second Detail of Precision Processed Scene 1062-15190-5.	4-13
4.10 Power Spectral Density of Image Shifted One-half Pixel..	4-14

LIST OF TABLES

2-1 ERTS-1 Spectral Band Assignment	2-2
2-2 Typical GCP Extraction Precision	2-8
2-3 Position Error Data for Scene 1057-18172.....	2-19
2-4 PASS-I Error Budget	2-22
2-5 Module Throughput	2-29
3-1 Module Throughput	3-14

LIST OF ABBREVIATIONS AND SYMBOLS

AMS	Attitude measurement sensor
BIAT	Bulk image annotation tape
CCT	Computer compatible tape
GCP	Ground/geodetic control point
ICT	Image center time
MSS	Multispectral scanner
RBV	Return beam vidicon
S/C	Spacecraft
USGS	U. S. Geological Survey
UTM	Universal Transverse Mercator
ϕ	Geocentric latitude
λ	Longitude
ϕ_i	Latitude coefficients
λ_i	Longitude coefficients
h_i	Altitude coefficients
ω_e	Earth rotational rate
t	Time
r_e	Earth equatorial radius
R_x, R_y, R_z	ECI position coordinates
$\dot{x}, \dot{y}, \dot{z}$	ECI velocity components
θ	Heading angle
$\underline{\theta}$	Vector of attitude time series coefficients
ξ	Scan advance coordinate
τ	Along scan coordinate
l	Line number
p	Pixel number
x, y	Corrected image grid coordinates
u, v	Bulk image grid coordinates
a_i, b_i	Distortion coefficients

LIST OF ABBREVIATIONS AND SYMBOLS (contd)

a	Earth semi-major axis
e	Earth eccentricity
β	Mirror scan angle
R, P, Y	S/C body coordinates
ER, EP, EY	Local attitude coordinates
\underline{u}	Unit scan vector
S	Meridinal arc
P	Covariance matrix associated with $\underline{\theta}$
k	GCP index
σ	GCP location accuracy
ϵ_p	Norm of GCP residual error

PREFACE

This is the final report on the Evaluation of Digital Correction Techniques for ERTS Images. This report fulfills the deliverable documentation requirements for Item 5, Contract NAS5-21814. Additionally, this report summarizes work completed since the last progress report.

During the course of the study, TRW has evaluated various digital correction techniques applied to bulk CCT MSS and RBV data in four primary areas:

- processing - induced distortions
- reseau and ground control point location accuracy
- geometric distortion correction accuracy
- throughput

TRWs CDC 6400 computer was utilized as the major tool in evaluating these techniques. The study was not explicitly concerned with image enhancement, but rather concentrated on the various elements of ERTS data processing. While the various tasks have not been combined to produce a contiguous data flow required in an operational facility, the processing modules described in this report have been evaluated individually in terms of throughput.

The principle performer of this study was Dr. S. Rifman, with Mr. J. Taber and Dr. K. Simon providing overall direction. Dr. Rifman was periodically supported by M. Benesch, A. Hung, D. McKinnon, J. Rau, W. Spence, and K. Ziedman. Ms. Benesch particularly made valuable contributions to the RBV effort. Dr. R. Caron provided helpful consultation for the Kalman Filter.

Deep appreciation is extended toward Mr. Bernard Peavey, the Science Monitor, who has provided much valuable support throughout this contract. Grateful thanks are due Messrs. Tom Burger and Mel Byerly of the U.S. Geological Survey who supplied the necessary precision geodetic ground truth data.

1

INTRODUCTION AND SUMMARY

1.1 STUDY SCOPE

The ultimate value of satellite-collected Earth resources data will depend on the speed and accuracy with which meaningful information can be extracted. TRW's study objective has been to verify that the prerequisite geometric and photometric correction of ERTS-1 MSS and RBV data can be speedily and accurately accomplished with all-digital image processing techniques.

TRW has studied several digital correction techniques and evaluated these techniques in four primary areas:

- processing-induced distortions
- reseau and ground control point (GCP) location accuracy
- Geometric distortion correction accuracy
- throughput

Processing-induced distortions include resolution degradation, corrected image discontinuities, and any artifacts. It is emphasized that this study was explicitly not concerned with image enhancement techniques; consequently, only resolution degradation and artifacts induced by the data processing were considered. The geometric distortion correction accuracy includes residual sensor distortions and attitude/ephemeris error-caused distortions. These are affected by the reseau and GCP location accuracies.

Due to the shutdown of the RBV shortly after ERTS-1 launch, processing priority was shifted to MSS data although considerable progress had already been achieved in adapting TRW algorithms to accommodate the RBV data. As a consequence, the bulk of this report is focused on the evaluation of MSS data processing techniques. Table 1-1 lists the images processed in the course of the study.

Table 1-1. NASA Imagery Processed in the Course of the Study

Sensor	NASA Scene No.	Geographical Description
RBV	1002-18134	Monterey Bay
MSS	1057-18172	San Pablo Bay
MSS	1062-15190	Baltimore/Washington
MSS	1080-15192	Baltimore/Washington

1.2 STUDY APPROACH

Evaluation of ERTS digital image correction techniques has proceeded in four stages:

- a. Adaptation of TRW algorithms to the ERTS data formats;
- b. Parametric design and performance evaluation;
- c. Performance evaluation of digital image corrections with data provided by NASA; and
- d. Determination of throughput for critical processing steps.

Specific algorithm areas for evaluation included:

- a. Evaluation of three interpolation techniques*
 - nearest neighbor interpolation
 - bilinear interpolation
 - TRW Cubic Convolution Process
- b. Kalman Filtering for precision attitude refinement (MSS only)
- c. Piecewise low-order distortion model*
- d. Spiral search and shadow casting for reseau location *
- e. Automatic GCP extraction via sequential similarity detection

In general, three approaches were employed for the evaluations: (a) automatic computer processing; (b) manual verification; and (c) visual inspection. Thus, evaluations of the geometric precision were assisted by computer processing for the rms differences between known ground locations and those determined from the corrected image (MSS and RBV), or by the rms differences between known reseau locations and those determined from the corrected image (RBV).

Processing-induced distortions, which manifest themselves as resolution degradation, image discontinuities and photometric errors were evaluated by means of statistical algorithms (histograms), spatial frequency analyses and visual inspection. Analyses of errors inherent in the image correction algorithm also will be presented.

*Developed prior to the commencement of this contract under company-sponsored programs.

Ground control point and reseau identification and location accuracy were evaluated by means of manual inspection and verification of photographic and printer/plotter imagery for the areas in question. The speed and effectiveness of algorithms for GCP identification were also considered. Finally, the overall throughput of the processing was evaluated for RBV and MSS imagery. Comparisons were made between several resampling algorithms and examples of running times are given for CDC 6400 computer processing.

The actual work progressed through three phases as illustrated in Figure 1-1. The first phase (pre-launch) was devoted to processing tool collection and modification. These tools were examined in the second phase with first-look ERTS-1 data, required tool modifications were initiated, and the compatibility of TRW's processing/evaluation techniques with ERTS-1 data was established. The second phase was concluded with the publication of the Data Analysis Plan for Phase III, the continuing data analysis phase. Phase III consisted of two principal facets: a) precision processing of selected imagery, and b) evaluation of the spatial and photometric properties of the processed imagery from the standpoint of precision and throughput. Results of the Phase III studies are documented in this report.

A top-level functional flow of the software tools utilized by TRW to process RBV and MSS data appears as the two step procedure illustrated in Figure 1-2. The first step, referred to herein as Pass I, includes the image distortion estimation function, the data reformatting function for bulk CCT data supplied by NASA/NDPF, and the GCP/reseau search region extraction function. The distortion estimation function results in the generation of a data file of distortion coefficients, corresponding to the piecewise bilinear distortion model employed. The second data pass corrects the reformatted bulk CCT data pixel by pixel, using one of three processes identified at the beginning of this section, making use of the distortion coefficients generated in the first pass processing.

1.3 SUMMARY OF MAJOR RESULTS

TRW has employed highly efficient digital techniques to precision process bulk ERTS data. These techniques were utilized for:

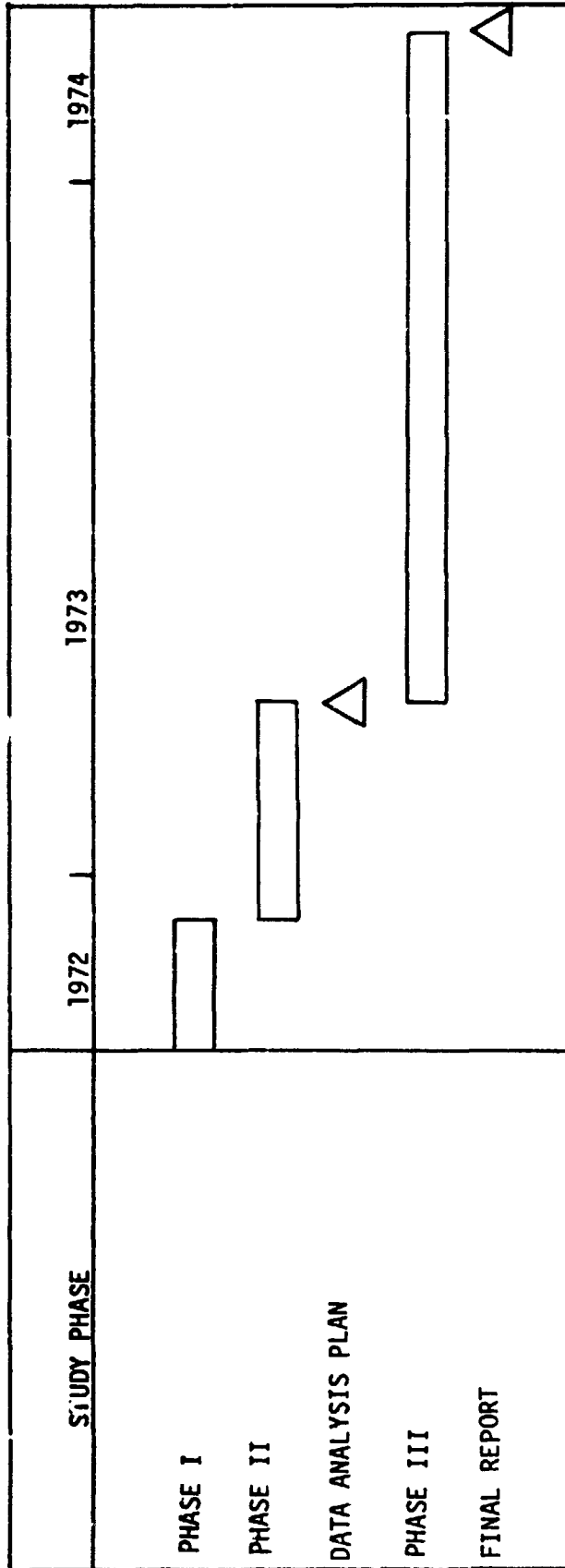


Figure 1-1. Study Schedule

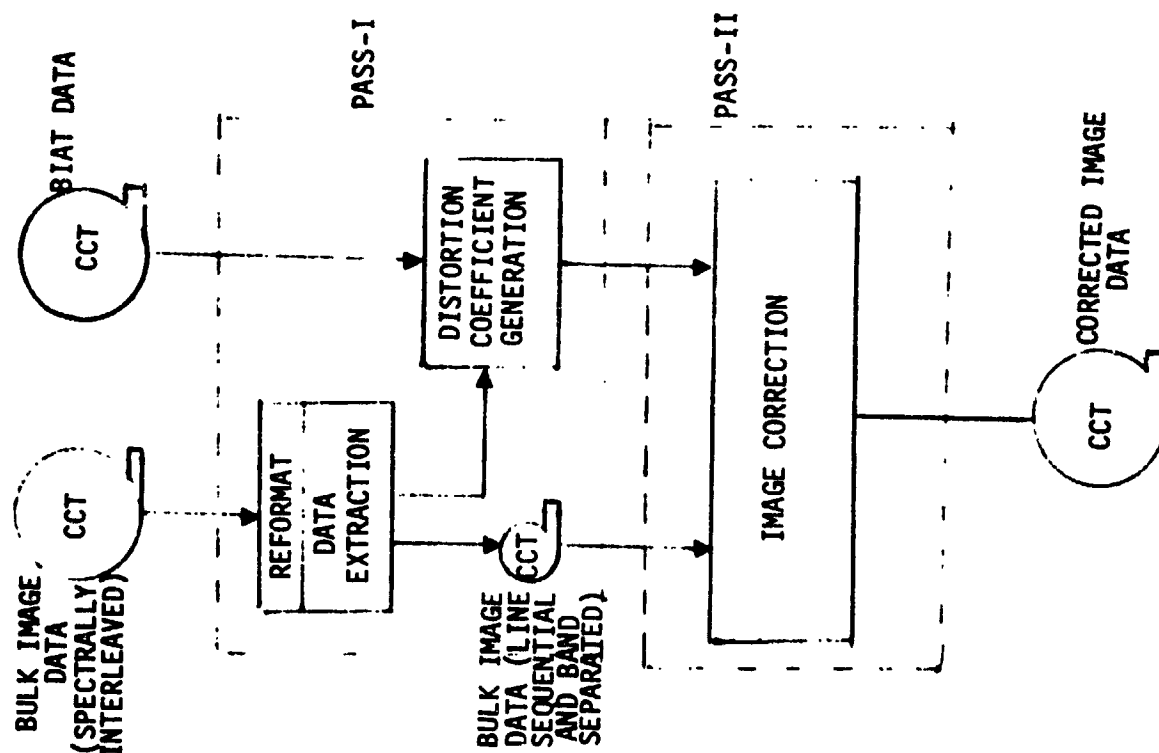


Figure 1-2. Top-Level Functional Flow for ERTS Data Processing

SENSOR CHARACTERISTICS IMPACTING RBV/MSS SOFTWARE DESIGN		
RBV	MSS	
INSTANTANEOUS IMAGE	25 SECONDS TO SCAN AN IMAGE	
OPTICAL DISTORTIONS	MIRROR SCAN AND ATTITUDE RATE DISTORTIONS	
REGISTRATION OF DATA FROM 3 SPECTRAL BANDS IS NOT INHERENT	INHERENT REGISTRATION OF ALL SPECTRAL BANDS	

- Automatic GCP Extraction
- Automatic Reseau Extraction (RBV only)
- Kalman Filter Attitude Refinement (MSS only)
- Piecewise Low Order Distortion Calculation
- Image Correction.

Both accuracy and throughput have been evaluated.

Automatic GCP Extraction

TRW has implemented an efficient technique which rapidly rejects mismatches between a reference image subarea (32 pixels x 32 lines) and a test segment of the same size derived from a larger search region (150 pixels x 120 lines). No positional errors were found when the reference subarea and search region were derived from the same ERTS bulk scene data. For search and reference data derived from two different orbital pass (i.e., 18 days or more apart in time), the maximum positional error was found to be 1 pixel. Running time on a CDC 6000 series computer averages about 14 sec./GCP.

Automatic Reseau Extraction

TRW has implemented a reseau search technique which searches most probable reseau locations first. This is done in two ways: 1) ordering reseaux to be extracted in a sequence corresponding to increasing image distortion, i.e., center reseau in each row first, followed by next adjacent pair of reseaux, etc.; 2) spiral search of each reseau search region (240 pixels x 240 lines) initiated at the position the reseau was last found (in the same or adjacent row), or at the position expected from pre-flight calibration measurements. This search is followed by thresholded shadow casting (row and column summing of image data) to locate the reseau center. Precision to a fraction of a pixel is derived from a polynomial fit to the shadow values. Incrementing the shadow threshold permits extraction of even low contrast reseaux.

All reseaux extracted were correctly located, to the accuracy of independent measurement techniques utilizing line printer output. No false detections were experienced. Average time to extract a reseau was \approx 4 sec of CPU on a CDC 6400 computer for a search region 240 pixels x 240 lines.

Kalman Filter Attitude Refinement

The Kalman Filter was implemented in the form of an optimum linear attitude estimator, driven by errors in the UTM plane between actual GCP locations (obtained from the U.S. Geological Survey) and estimated GCP locations, using the BIAT data for initial attitude estimates. Only 3 GCPs were required to reduce residual errors to one pixel, a limiting value determined by the GCP extraction precision and sensor IFOV. CPU time for a CDC 6400 was 4.1 sec.

Piecewise Low-Order Distortion Calculation

For the MSS data it was found that a piecewise bilinear distortion model fit to 81 image positions (for which distortions were computed to high accuracy) is consistent with absolute worst case modeling errors $\leq .5$ pixel. Highly accurate models for the sensor scan and spacecraft attitude and ephemeris are utilized to compute the resultant distortion coefficients for 8x8 regions spanning a scene, 8 coefficients per region. Distortion coefficient calculation for one MSS scene requires 20 sec of CPU exclusive of GCP extraction. Output corrected imagery is projected in a UTM coordinate system.

RBV image distortions were also successfully modeled by means of a piecewise bilinear model, utilizing 36x36 search regions. Modeling errors in this case were ≤ 1 pixel, and CPU time was about 44 sec, inclusive of reseau extraction, and exclusive of GCP extraction.

Image Correction

Precision correction of image data was accomplished by means of: 1) nearest neighbor interpolation, 2) bilinear interpolation, and 3) TRW Cubic Convolution Process, developed by TRW prior to the commencement of this contract. It was found that both nearest neighbor and bilinear interpolation processes significantly degraded image quality, whereas TRW Cubic Convolution generated the most satisfactory results. Thus, for example, nearest neighbor interpolation produced one pixel discontinuities, noticeable throughout the image. Bilinear interpolation was free of the image discontinuities produced by nearest neighbor interpolation, but noticeably degraded image resolution (spatial frequency content). Image data processed by the TRW Cubic Convolution Process had neither the nearest-neighbor discontinuities nor the loss of spatial frequency content occasioned by bilinear interpolation. Furthermore, comparison of TRW's digitally processed

ERTS imagery with current NASA precision products reveals the superior quality of the digital processed result to the analogue method (scan/rescan).

CPU time for the nearest-neighbor interpolation process was fastest (about 25 sec/ 10^6 pixels), was intermediate for bilinear interpolation (about 56 sec/ 10^6 pixels), and for TRW Cubic Convolution was slowest (about 110 sec/ 10^6 pixels) for the three processes considered. This corresponds to a range of 12.5 minutes - 55 minutes for a full ERTS scene (4 bands, or a total of 30×10^6 pixels of output data) using a CDC-6400.

1.4 CONCLUSIONS AND RECOMMENDATIONS

TRW has developed and demonstrated all-digital techniques to precision process ERTS imagery. Extension of the large-scale computer implementations to small-scale "minicomputer" configurations should ultimately result in a highly cost effective implementation (in fact at least one minicomputer offers a factor of two improvement in throughput over the CDC 6400 system utilized in this study). It is recommended that this approach be pursued, and that simultaneously efforts be undertaken to extend the existing techniques to permit registration of data from different 18-day S/C passes to a fraction of a pixel. This will make possible change detection studies directly from digitally processed data.

1.5 PUBLISHED PAPERS

References (5), (6), (7) cite the papers published during the course of this contract.

1.6 NEW TECHNOLOGY

No new technology was discovered during the course of this contract.

2

MSS DATA PROCESSING

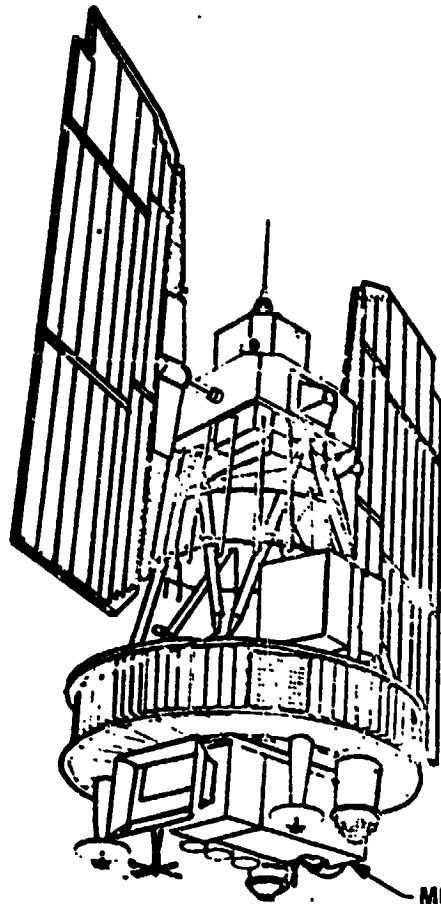
2.1 INTRODUCTION

The Multispectral Scanner Subsystem (MSS) gathers data by imaging the surface of the earth in several spectral bands simultaneously through the same optical system. The MSS for ERTS-1 is a 4-band scanner operating in the solar-reflected spectral band region from 0.5 to 1.1 micrometer wavelength. It scans cross-track swaths of 185 kilometers (100 nm) width, imaging six scan lines across in each of the four spectral bands simultaneously. The object plane is scanned by means of an oscillating flat mirror between the scene and the double-reflector, telescope type of optical chain. The 11.56 degree cross-track field of view is scanned as the mirror oscillates ± 2.89 degrees about its nominal position as shown in Figure 2.1 (Reference (2)). Table 2-1 lists the spectral bands for ERTS-1.

The instantaneous field of view (IFOV) of each detector subtends an earth-area square of 79 meters on a side from the nominal orbital altitude. Across scan separation of IFOV's is approximately the same, but the separation along scan is approximately 56 nm.

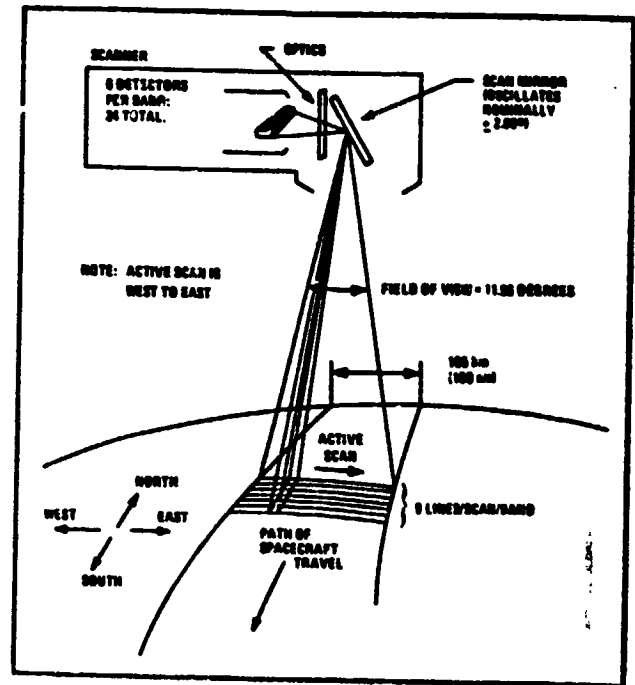
Table 2-1. ERTS-1 MSS Band Assignment

<u>Band</u>	<u>Wavelength</u>
Band 1	0.5 to 0.6 micrometers
Band 2	0.6 to 0.7 micrometers
Band 3	0.7 to 0.8 micrometers
Band 4	0.8 to 1.1 micrometers

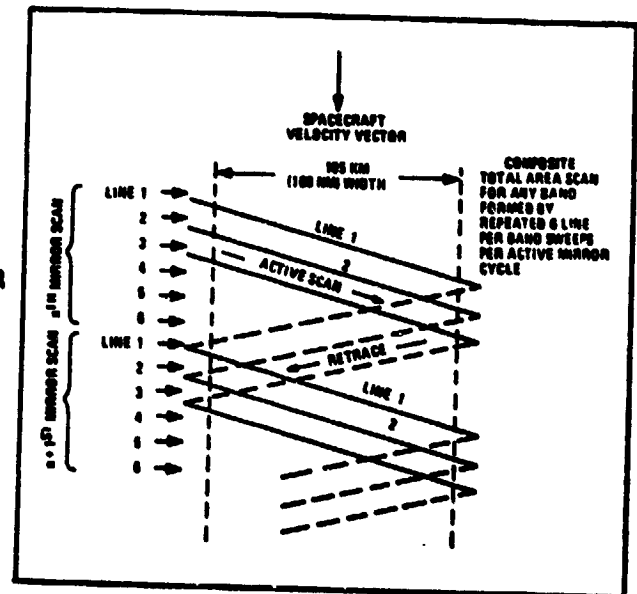


MULTISPECTRAL SCANNER

SOURCE: REFERENCE 2



MSS Scanning Arrangement



Ground Scan Pattern
for a Single MSS Detector

Figure 2.1. MSS Subsystem

The sampling interval is 9.95 μ sec, corresponding to a cross-track motion of the instantaneous field of view of 56 meters. The along-track scan is produced by the orbital motion of the spacecraft. By oscillating the mirror at a rate of 13.62 Hz, the subsatellite point will have moved 474 meters along-track during the 73.42 millisecond active scan and re-trace cycle. The width of the along-track field of view of six detectors is also 474 meters. Figure 2.1 shows the composite scan pattern.

The downlinked MSS data is processed by the NASA Data Processing Facility (NDPF) to produce film products and Computer Compatible Tapes (CCT). Four CCT's are required for the digital data corresponding to one scene, framed 185 Km on a side. The MSS data on the CCT's is spectrally interleaved, line-length adjusted, and radiometrically calibrated. For a given spectral band, one active scan of the MSS mirror produces simultaneously six lines of bulk image data. A total of 2340 lines (390 scans) constitute one such image. For each set of images there is a set of S/C ephemeris and attitude data, relative to the time of the image center point (image center time, ICT), recorded on the bulk image annotation tape (BIAT).

TRW's first pass program for multispectral scanner data is called MSS. MSS is a CDC 6400 program encoded in modular manner to flexibly exercise PASS-I algorithms.

2.2 METHODOLOGY

The function of the MSS program is to generate a file of distortion coefficients representing the geometric correction transformation which maps the bulk image to the geometrically corrected output image in a UTM projection. The geometric distortions of the MSS bulk image are due to errors in the vehicle attitude/ephemeris which may vary from scan to scan, to irregularities in the motion of the scanning mirror, and to earth curvature and rotation. A schematic of the MSS software is given in Figure 2.2.

The determination of the distortion coefficients requires accurate models for the sensor scan and the vehicle attitude/ephemeris. Initial values of spacecraft attitude, altitude, and nadir attitude and longitude

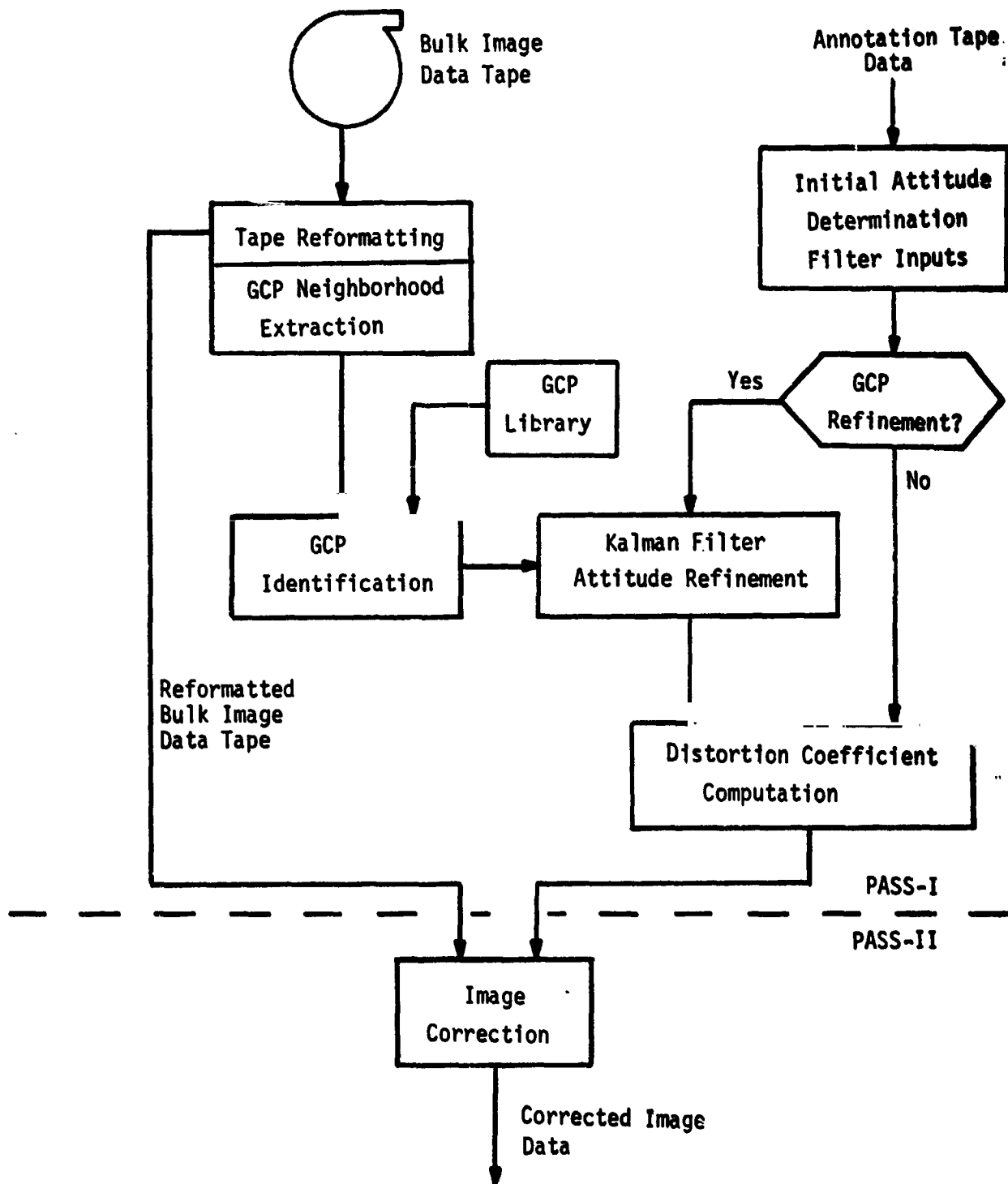


Figure 2.2 MSS Program Functional Schematic

are provided on the annotation tape for 9 equally-spaced points spanning an image. These values are least-squares fit to corresponding cubic polynomials in time to develop an initial estimate of the vehicle attitude/ephemeris. The attitude data is then refined, on option, by determining positions of selected Ground Control Points (GCP's) on the input CCT, and employing a Kalman filter for a precision refinement of the roll, pitch, and yaw coefficients.

Given the refined (or initial) attitude profile, the image distortion coefficients are computed by first defining a regular grid of image locations, called "pseudo-reseaux," in the coordinate system of the bulk image. These points are mapped to their corresponding locations in UTM coordinates in the corrected image coordinate system. The LOS vector from the spacecraft is determined for each pseudo reseau point as a function of time through the use of analytical models of the earth-vehicle system and the MSS mirror scan.

A regular grid of pseudo-reseaux is then defined in the UTM system parallel to the spacecraft ground track and centered with respect to the initial set of pseudo-reseaux mapped from the bulk image system by means of a least-squares fit of the edge reseaux. The distortion coefficients (defined for each block of four pseudo-reseaux in the regular UTM system) are computed on the basis of a bilinear distortion model, through an inverse mapping from the regular reseau coordinate system to the bulk image (uncorrected) coordinate system. This mapping is accomplished by means of a rapidly convergent iterative technique.

2.3 MSS DATA PROCESSING RESULTS

The results of the evaluation of TRW algorithms for processing MSS data encompass five areas: GCP extraction precision, Kalman filter performance, Pass I precision, resampling algorithm comparisons, and module throughput.

2.3.1 GCP Extraction Precision

GCP search regions called "neighborhoods" (see Figure 2.3) were

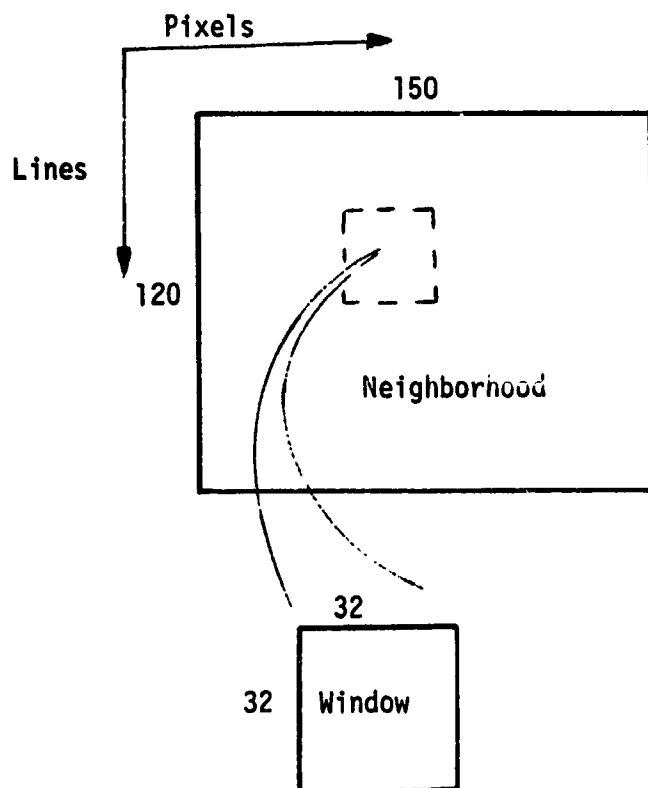


Figure 2.3. GCP Window Extraction from a Search Neighborhood

Dimensions refer to line and pixel values in bulk CCT data. A window is located within a neighborhood when the cumulated pixel value differences (random pixel ordering) within an overlap region (shown dotted above) do not exceed a moving threshold. A possible location is rejected quickly when the cumulated difference exceeds the same threshold, after a pre-determined number of differences are cumulated.

extracted as part of the bulk data reformatting process^{*}, which produces line sequential and band separated bulk image data. GCP location within each search region is accomplished by means of a feature matching technique (Reference (2)) which rapidly rejects mismatches.

Typical of the precision of the technique are the results given in Table 2-2. Four tests were made using scene 1062-15190-5 and scene data obtained 18 days later, 1080-15192-5. For simplicity, let scene 1062-15190-5 be denoted as 62, and let scene 1080-15192-5 be denoted as 80; let N (neighborhood) represent the search region, (150 pixels x 120 lines), and let W (window) represent the reference template of the GCP (32 pixels x 32 lines).

The intersection of Interstate 83 and the Baltimore Beltway stands out clearly in both scenes and was taken as the GCP. The tests consisted of utilizing: a) 62 as the window data (62W), and 80 for the source of neighborhood data (80N); b) 62 as both sources for window and neighborhood data (62W + 62N); c) 80 as both sources for window and neighborhood data (80W + 80N); and d) the reverse of the first case (80W + 62N). The parameter XNOISE is the threshold increment used to compute the threshold JT. Basically, a large XNOISE will give a large probability of false detection and cause the algorithm to run slower, while a small XNOISE will give a large probability of false rejection and cause the algorithm to run faster. For $XNOISE=4^{**}$, the mean time to extract a GCP is 19.2 cpu seconds, and the errors for 62W + 80N and 80W + 62N reach a minimum value.

Observations made subsequent to these tests indicate that a one pixel error can occur if the feature in question has been nearest-neighbor line length adjusted, i.e., a replicated pixel is present (Reference (3), Appendix 2).

^{*} Using CDC computers necessitated conversion to 6 bit data per pixel at the same time.

^{**} Out of a possible range of 64, for 6 bit data.

Table 2-2. Typical GCP Extraction Precision

WINDOW + NEIGHBORHOOD	XNOISE	TIME TO EXTRACT GCP (cpu sec)	ERROR	
			LINES	PIXELS
62W + 62N	1	4.8	0	0
	2	5.5	0	0
	3	7.9	0	0
	4	9.6	0	0
80W + 80W	1	5.1	0	0
	2	7.2	0	0
	3	11.2	0	0
	4	25.0	0	0
62W + 80N	3	6.8	18	32
	3.5	8.3	-28	-36
	4	13.3	-1	-1
	5	44.1	-1	-1
	6	> 60	--	--
80W + 62N	3	8.9	12	36
	4	15.0	0	0
	4.5	34.5	0	0
	5	> 60	--	--

NOTE: In no case was an error in GCP location encountered when the GCP window was extracted from the neighborhood in question. Error sources for neighborhoods and windows derived from different scenes include: a) scene photometry differences, related to the seasonal variation in solar elevation angle; b) changes in vegetation with season (brown and green waves); c) line length correction differences between two scenes, involving the nearest-neighborhood replicated pixel occurring in the feature for only one of the two scenes.

2.3.2 Kalman Filter Performance

The precision rectification of an ERTS/MSS bulk image requires an estimate of the ERTS attitude time-series over the time interval in which the image was scanned. Such an estimate can be obtained by fitting polynomials to the sampled attitude data on the Bulk Image Annotation Tape (BIAT). Unfortunately, an attitude time-series obtained in this way does not meet the stringent requirements of precision image rectification. To achieve image rectification on the order of 1 pixel, it is necessary to know each attitude component to within $\pm .01$ milliradians. According to the ERTS Data User's Handbook (Reference (1)), the ERTS attitude measurement system is accurate only to the nearest milliradian. Clearly, some additional information is required to obtain a more refined estimate.

Since the attitude data available from the annotation tape corresponds to a limited number of values, the MSS program utilizes a Kalman filter to update the initial estimates of attitude coefficients using Ground Control Points. When this option is selected, the Kalman filter subroutine updates the attitude coefficients given the initial coefficients (state vector), the error covariance matrices for each component, and the differences in GCP ground locations (known a priori location minus that computed from the bulk image).

The estimator was implemented on the CDC 6400 computer using data derived from ERTS/MSS bulk image, 1062-15190 (1068-35:BIAT). For the image considered, it was shown that only 3 Ground Control Points are required to drive the Ground Control Point position estimation error from 4.5 kilometers to less than 80 meters. This result suggests that the estimator is performing up to the resolutional capability of the MSS detectors. GCP's were selected from a list supplied by USGS and 7.5 minute quadrangle maps provided by USGS. References (6) & (8) describe TRW's 2-dimensional UTM observable estimator. Let the ERTS attitude time-series (restricted to the image time interval) be represented by $\underline{\theta} = (\underline{\theta}_r, \underline{\theta}_p, \underline{\theta}_y)$ whose sub-vector components are comprised of sets of coefficients which define polynomial realizations of the roll, pitch, and yaw time series. Let σ represent how well the ground truth points are known.

The prior estimate of $\underline{\theta}$ is derived from attitude-sampled-data on the BIAT. Figures 2.4, 2.5, and 2.6 show the results of least-squares fitting 1st, 2nd, and 3rd order polynomials to each set of sampled-data. These figures demonstrate the sufficiency of a third-order polynomial representation for each of the attitude components.

Due to the unavailability of statistics, the a priori covariance matrix $P(o)$ and the GCP location accuracies $\sigma(k)$, $k=1,2,\dots$, were assigned on a subjective basis. The selection of $P(o)$ was circumscribed by the following assumptions:

- 1) The components of $\underline{\theta}$ are uncorrelated.
- 2) The uncertainty in the zeroth order component of $\underline{\theta}$ ($\alpha \in \{r,p,y\}$) is bounded by the attitude measurement^a uncertainty specified by NASA (1.2217 milliradians).
- 3) Uncertainty in the j^{th} order component of $\underline{\theta}$ ($j=1,2,3; \alpha \in \{r,p,y\}$) does not exceed 10% $\frac{\sigma}{\theta}$ of the absolute value of the component's initial value.

On the basis of these assumptions, $P(o)$ was taken to be diagonal with

$$(P(o))_{ii} = S^2_{(i-1)\text{mod}(4)+1} \quad i=1,2,\dots, 12$$

$$S_1 = 1.22173 \times 10^{-3}, S_2 = 10^{-7}, S_3 = 10^{-8},$$

$$S_4 = 10^{-10}.$$

For GCP's not obscured by cloud cover, σ was assigned a value of 30 meters.

The filter representation shown in the appendix is that of an operational implementation. Classically, the state update is written:

$$\underline{x}_{\text{NEW}} = \underline{x}_{\text{OLD}} + A(\underline{y} - \underline{y}_{\text{TRUE}})$$

where A is the gain matrix and the \underline{y} vectors are GCP locations. The norm of the GCP residual error, $\underline{y} - \underline{y}_{\text{TRUE}}$, was found to be a useful measure of filter stability. Intuitively, the norm should decrease with increasing observations of GCP's if $\underline{\theta}$ (estimate of $\underline{\theta}$) is stable. Figure 2.6 indicates this behavior for 10 GCP's.

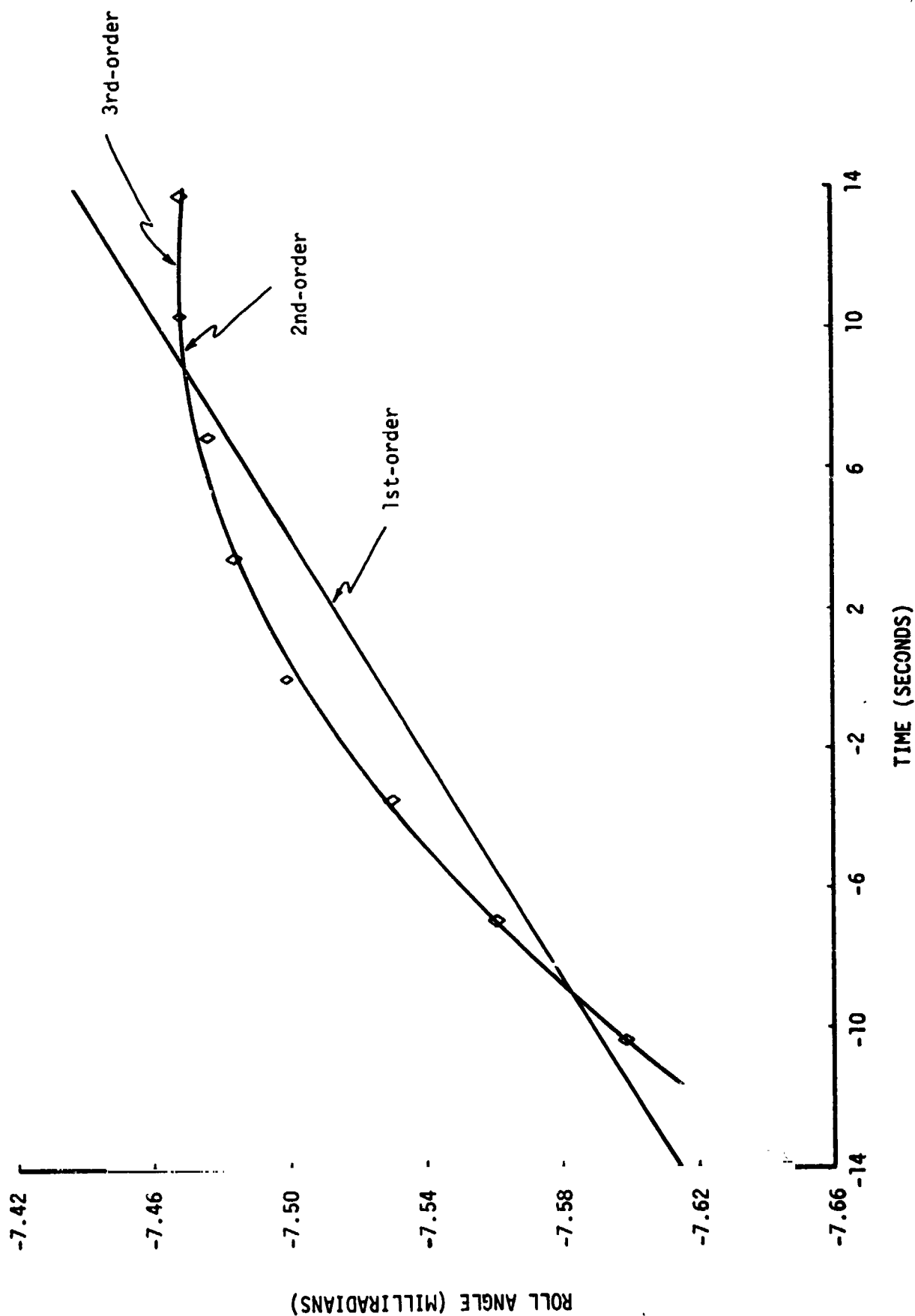


Figure 2.A Polynomial Models of Roll Time-Series

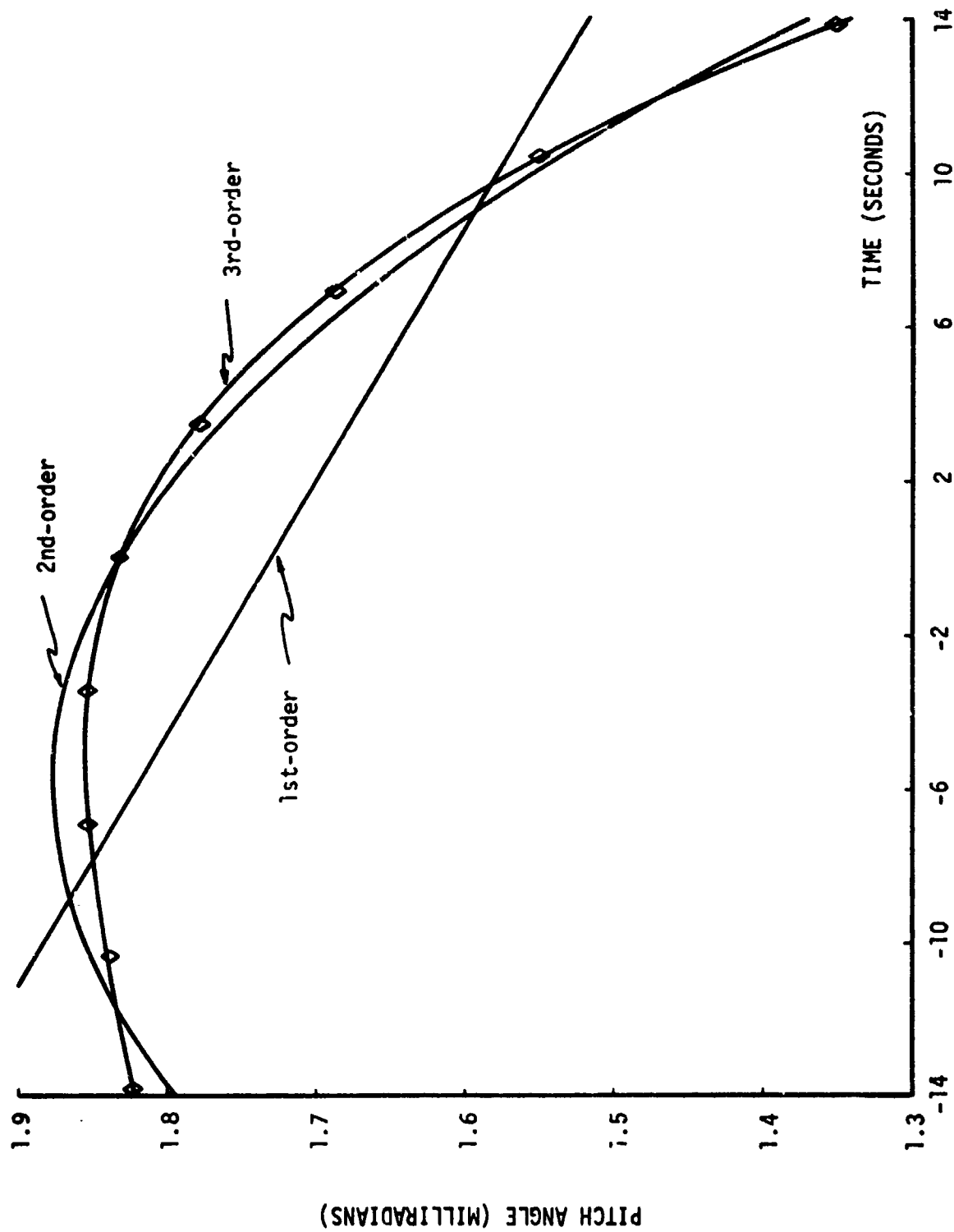


Figure 2.5. Polynomial Models of Pitch Time-Series

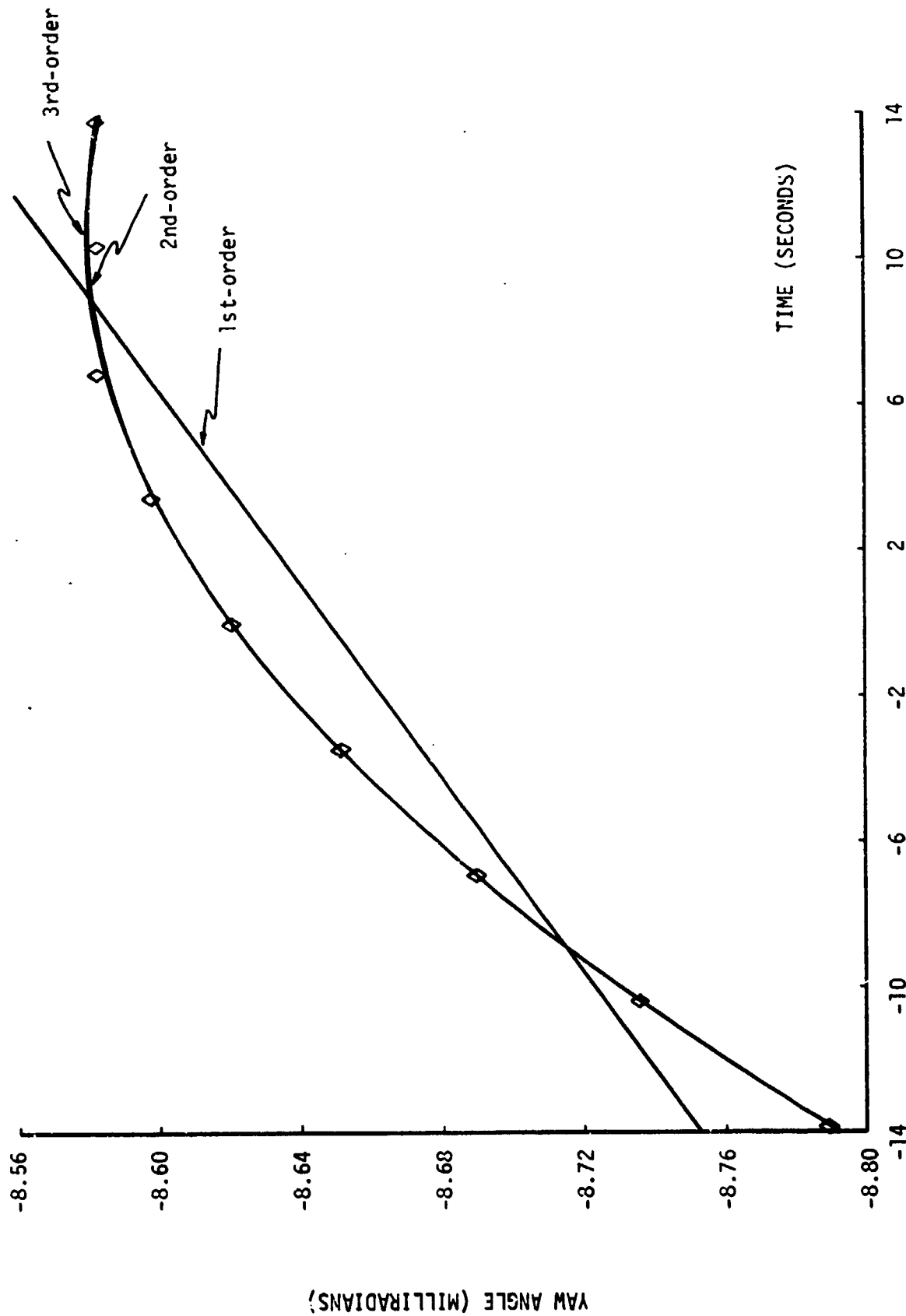


Figure 2.6. Polynomial Models of Yaw Time-Series

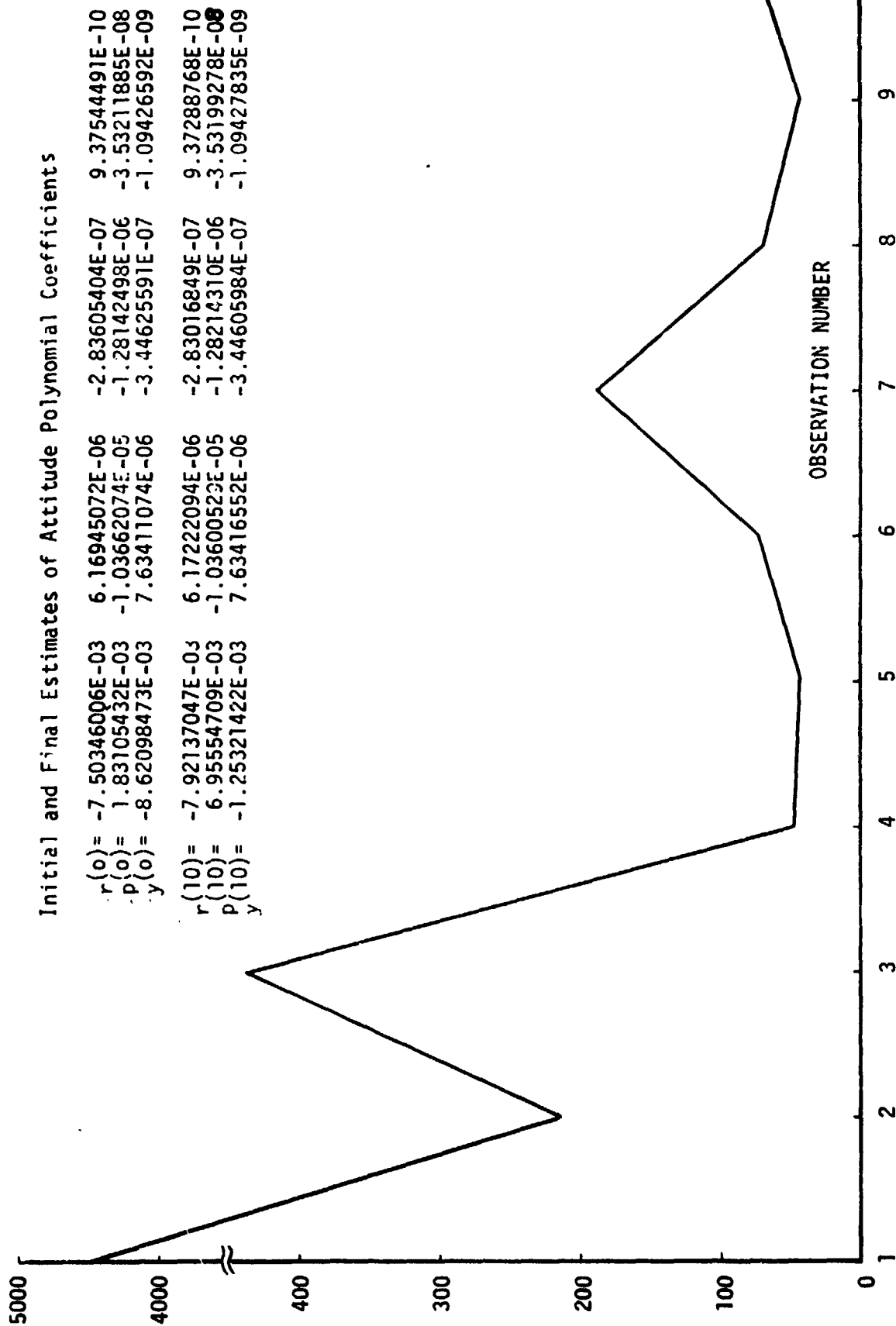


Figure 2.7. Norm of GCP Residual Error Vs GCP Observation Number

Another measure of $\hat{\theta}$'s stability is the behavior of the zeroth order error-covariance terms as a function of observation number. Plots of the square roots of these functions (Figure 2.8), exhibit a highly stable monotone decreasing behavior which tends to be asymptotic to zero. Notice that after 10 GCP's, the roll and pitch estimates have converged to within $\pm .01$ milliradians of their true values, whereas the yaw estimate converges to within $\pm .28$ milliradians of its true value.

Comparison of the norms before and after filtering provide a measure of the filter's worth. Before filtering there is a persistent error on the order of 4.5 kilometers; but after filtering, the error is on the order of 79 meters (1 pixel), suggesting that the estimator is performing to the limits of the sensor IFOV and GCP location accuracy.

Figure 2.9 shows the accuracy of the estimator as a function of the number of observations, $k=1, 2, \dots, 10$. After the k^{th} observation, the resulting $\hat{\theta}(k)$ was used to compute the norm for all observations and a mean standard deviation were computed (sample size=10). The plots in Figure 2.8 show the results of repeating this process for $k=1, 2, \dots, 10$. The figure shows that only three GCP's are required to correct the attitude time-series to one GCP, since the attitude uncertainty is zeroth order, as evidenced by comparing the initial and final estimates of θ given in Figure 2.7.

2.3.3 Pseudo-Reseau Grid Modeling Errors

Corrections for geometric distortions in the MSS image are obtained by calculating exact corrections for a subset of image points (pseudo-reseau points) and applying a piecewise bilinear distortion model to determine corrections for all other points. The accuracy of the piecewise model increases as the number of pseudo-reseaux is increased; however, processing time also increases. The relationship between number of pseudo-reseaux and positional error was investigated to permit selection of pseudo-reseau grid size to meet a desired error criterion.

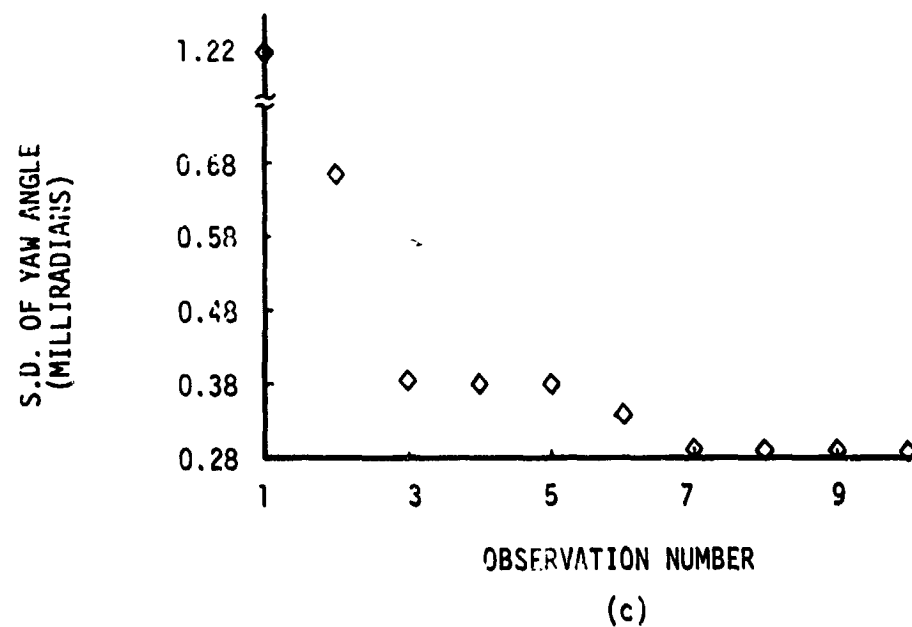
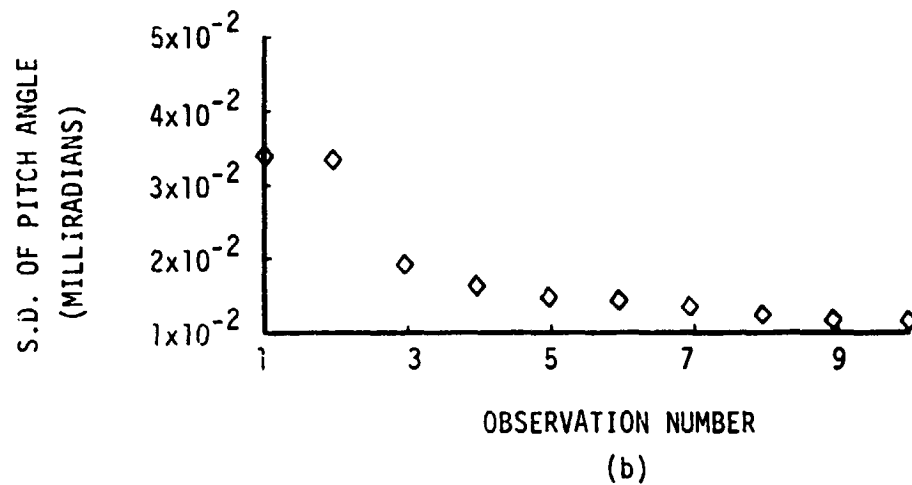
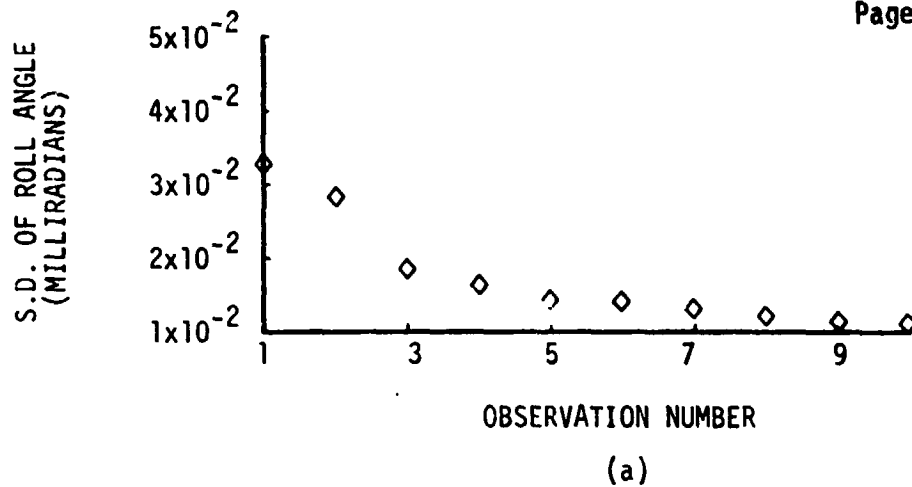


Figure 2.8. Attitude Estimation Uncertainty

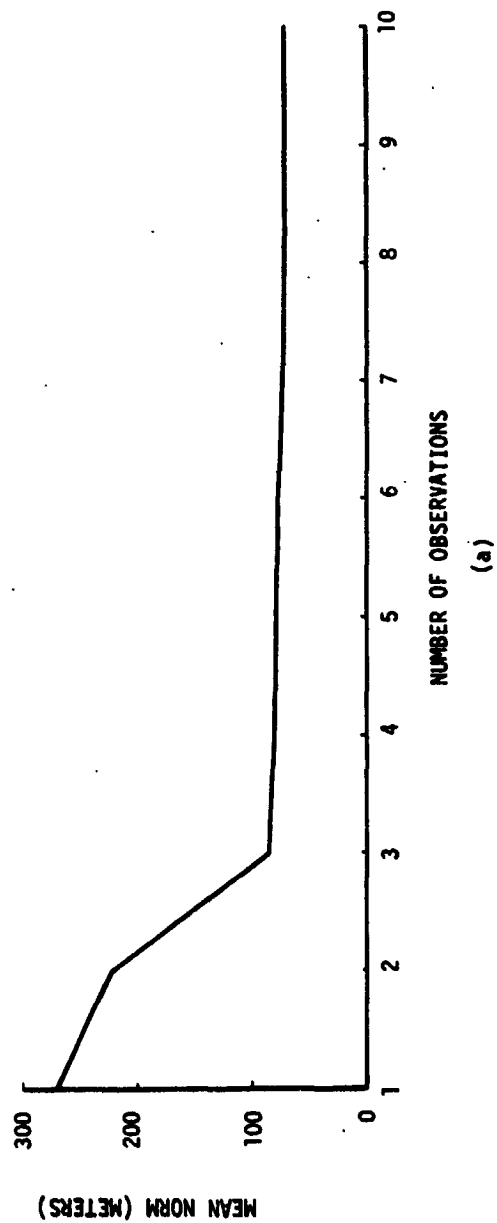
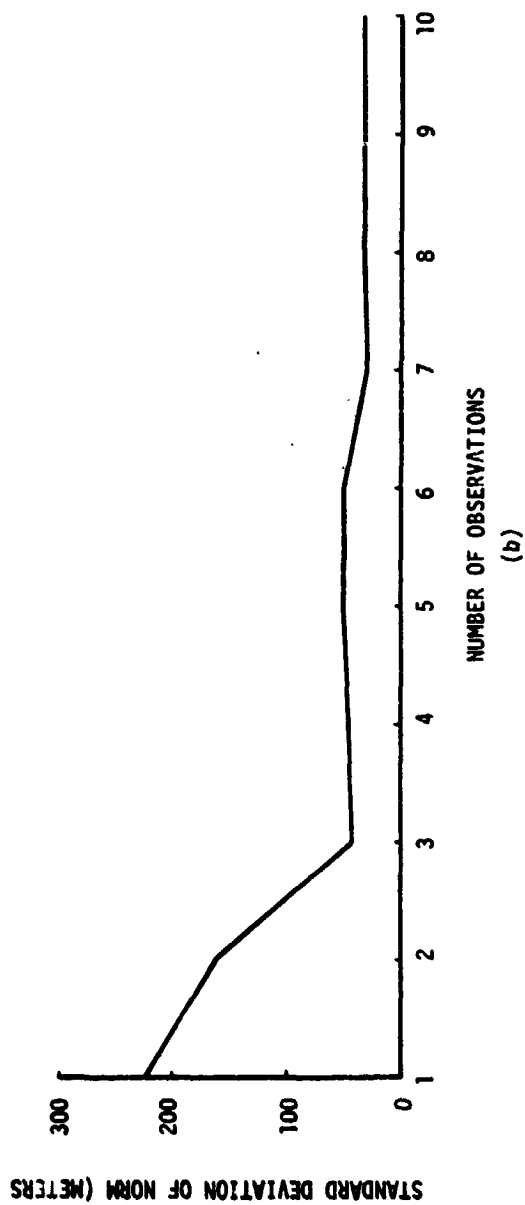


Figure 2.9. Statistics Based on a Sample of 10 GCP's

The MSS Pass I program was modified as follows:

- 1) The Ground Control Point (GCP) and Kalman filter routines, ordinarily used for attitude refinement, were deleted.
- 2) A provision for inputting "test points" was added (a test point is a pixel for which the error is to be determined).
- 3) The exact projection of each test point onto the output space was determined using the existing subroutines.
- 4) An additional subroutine was added to perform the bilinear interpolation for arbitrary pixel locations.
- 5) The difference between the exact projection and interpolated position of each test point was taken as the error.
- 6) Summary statistics for the errors are calculated.

Modeling errors were studied by (1) systematically scanning the image to locate the actual maximum error; and (2) randomly selecting test points ($N=200$) to obtain frequency distributions of errors as well as values for mean errors and standard deviations. Several measures were calculated: mean error, mean absolute error, maximum error from the systematic scans, maximum error from the random selections, error standard deviation σ , mean absolute error $+2\sigma$, and the error frequency distribution. Errors were measured separately in the line and pixel directions.

The principal results are shown in Table 2-3 for pseudo-reseau grid sizes ranging from 5×5 to 13×13 points. If a maximum (worst case) allowable position errors are on the order of 0.5 pixel or 0.5 line, the results indicate that a 9×9 pseudo-reseau grid is required. Further, it seems unlikely that a grid smaller than 7×7 (maximum errors on the order of 1.0 pixel or line) or greater than 11×11 (100% of errors less than 0.4 pixel or line) would be considered. Note that mean absolute errors are substantially smaller than the maximum errors and that the absolute error mean $+2\sigma$ values ($\pm 2\sigma$ about the mean is a 95% confidence limit, assuming a normal error distribution) agree fairly well with the actual maximum values obtained, whether from the random selection or systematic scan methods.

Table 2-3. Position Error Data for Scene 1057-18172

PSEUDO-RESEAU GRID SIZE* (AS) x (SA)	ERROR TYPE	MEAN ABSOLUTE ERROR	σ	MAXIMUM ERROR (RANDOM/SYSTEMATIC)	MEAN + 2σ
5 x 5	PX	.40	.49	1.26	1.38
	LN	.43	.55	1.28	1.53
7 x 5	PX	.21	.26	0.64	.85
	LN	.41	.51	1.26	1.43
7 x 7	PX	.23	.26	.54	.75
	LN	.22	.28	.73	.78
7 x 9	PX	.21	.26	.79	.73
	LN	.11	.15	.39	.50
9 x 7	PX	.13	.13	.39	.39
	LN	.22	.28	.71	.78
9 x 9	PX	.14	.16	.55	.46
	LN	.12	.15	.39	.42
11 x 9	PX	.11	.14	.47	.39
	LN	.11	.14	.39	.39
11 x 11	PX	.14	.11	.33	.36
	LN	.09	.10	.38	.29
13 x 13	PX	.08	.10	.29	.28
	LN	.06	.08	.26	.22

NOTE: Grid dimensions are given as Along Scan (AS) x Scan Advance (SA).
Errors are given in the Along Scan (PX) and Scan Advance (LN)
directions.

(The σ value was obtained from the algebraic error values.) The larger maximum random error or maximum systematic error is shown in Table 2-3.

A plot of the mean absolute errors and maximum errors as determined from the random test point runs is shown in Figure 2.10 for scene 1057-18172. The actual number of reseau blocks in the scan advance and along scan directions is given on the abscissa. In some cases, there are several points for a given number of reseau blocks as a given number of blocks in one direction was repeated while the number in the other direction was varied (e.g., 7 x 7 and 7 x 9 cases from Table 2-3. The along scan points show more variability than do the scan advance points, indicating that along scan interpolation errors for a given number of along scan blocks might be more sensitive to the number of scan advance blocks than vice versa. These curves can be used to predict (approximately), the error values for reseau sizes not included in this study.

Three grid sizes were run for a second picture, scene 1057-16375. The results indicate that the pixel error is about the same as for scene 1057-18172, but that the line error is greatly reduced. In general, maximum errors were found at the image corners. Within a pseudo-reseau block, maximum errors usually occurred in the vicinity of the center of the block.

Other variations were tried, including an azimuthal rotation of 0.5° , and an offset in the input grid origin from which the pseudo-reseau points are specified. None had an effect on error values. In summary, acceptable errors can be obtained with a reasonable number of pseudo-reseaux. The selection of a reseau grid will depend on the error size that is acceptable for a given purpose; a 9 x 9 grid would seem to be a good choice based on the images studied.

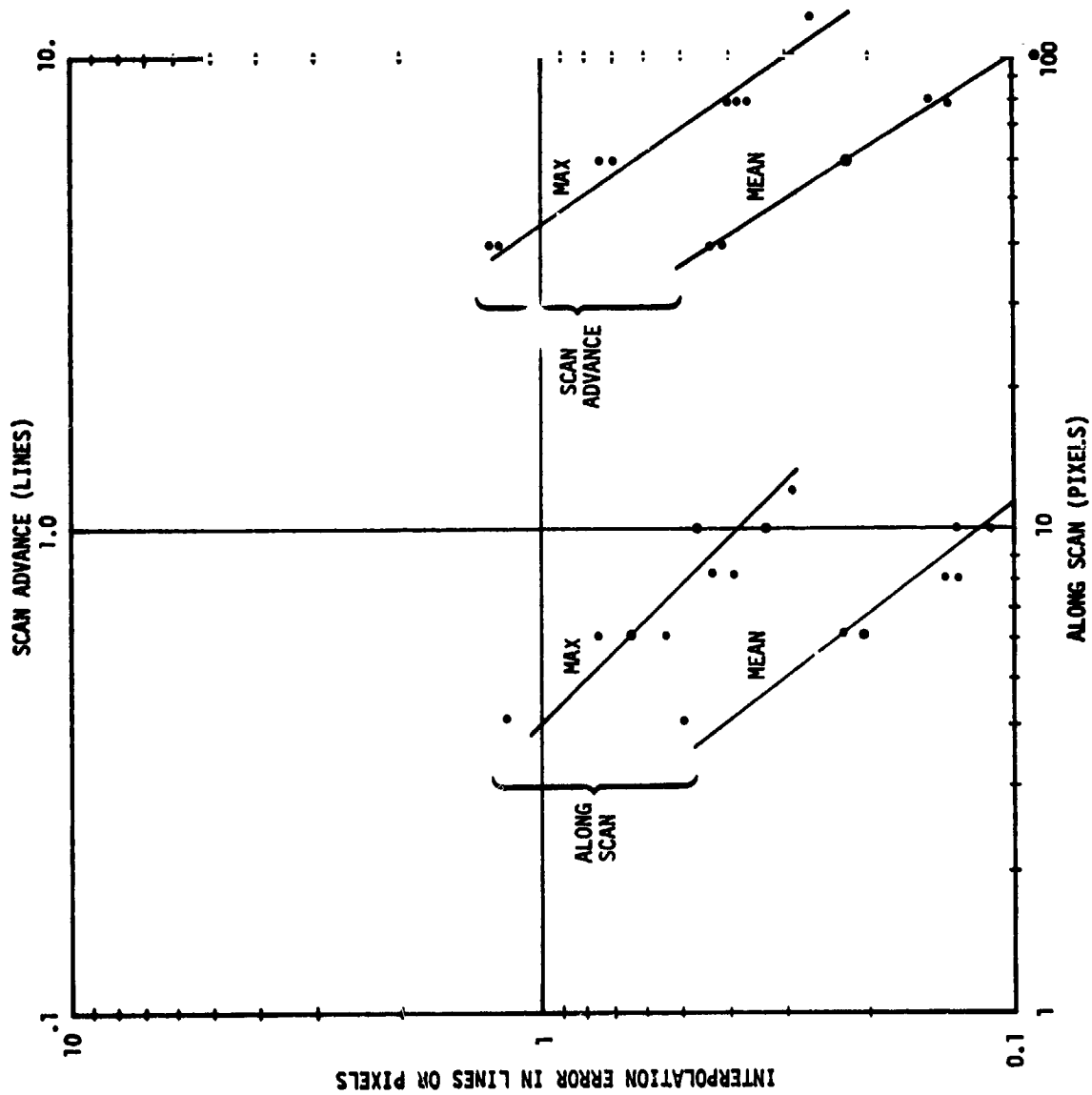


Figure 2.10. Mean Absolute and Maximum Random Position Errors

2.3.4 Pass I Precision

Using the results of the previous sections, it is possible to establish an error budget for the Pass I process. This budget is summarized in Table 2-4. Error sources modeled by the Pass I software elements include: spacecraft altitude variations within a frame; spacecraft attitude variations (roll, pitch, yaw) within a frame, earth rotation; spacecraft velocity changes; finite scan time effect; scan mirror velocity nonlinearities; perspective corrections; and bias errors due to MSS alignment to AMS.

Note that the GCP extraction error, while listed in the table, is not included in the computation of the RSS/RMS error. It is excluded since the GCP extraction error directly relates to the Kalman filter error--the filter will do no better than the GCP extraction accuracy. As a consequence, the Pass I RSS error is 1.12 pixels and the Pass I RMS error is 0.79 pixels.

Table 2-4. Pass I Error Budget

PASS I ELEMENT	MAXIMUM ABSOLUTE ERROR (Pixels)
GCP Extraction	1.0
Kalman Filter	1.0
Pseudo-Reseau Modeling	0.5
RSS	1.12
RMS	0.79

2.3.5 Processed Imagery

Typical of MSS image processing performance is scene 1062-15190, containing the cities of Baltimore and Washington, D.C. Figure 2-11 shows the bulk image for band 5 (red), the original negative for which was reproduced directly from NASA-supplied bulk CCT data, with no correction for aspect. Figure 2-12 is a NASA precision processed image for the same scene and band.* The loss of information proceeding from bulk CCT data to the NASA product is quite evident, and shall be made even clearer by the following figures.

Figures 2.13 and 2.14 show a detail (for bands 5 and 7, respectively) resulting from TRW's precision digital processing techniques and TRW's Cubic Convolution Process. The detail (scale $\sim 1: 571,000^{**}$) is centered around the city of Baltimore and its harbor. This region was selected instead of Washington because of the richness of detail and because silt in the Potomac resulting from storm activity reduced land/water contrast significantly (in the visible).

It is evident from Figure 2.14 at once that there is a considerable amount of detail in the digitally processed product. Note for example the runways of Baltimore-Washington International Airport (Friendship International), which are not evident in the NASA-precision product, an enlargement of which (band 7) is shown in Figure 2.15.

Additional MSS imagery was previously processed and reported on in the first 6-month report for this contract (Reference (8)) and in Reference (5). Comparisons between and analyses of three resampling methods are contained in Section 4 of this report, References (8) and (9).

* The original for this image was created as a contact negative from the NASA-supplied positive 9 1/2 inch transparency.

** On the original negative $100\mu = 57.098765m$.



Figure 2.11. Bulk Image 1062-15190-5 from CCT Data



Figure 2.12. NASA Precision Product for Image 1062-15190-5



Figure 2.13. Detail of TRW Precision Product for Image 1062-15190-5



Figure 2.14 Detail of TRW Precision Product for Image 1062-15190-7



Figure 2.15. Detail from NASA Precision Product for Image 1062-15190-7

2.3.6 Throughput

Table 2-5 summarizes the throughput characteristics for the several Pass-I MSS modules and the Pass-II algorithms implemented in FORTRAN on TRW's 6400. Times are given as central processor seconds. Pass-I executes under 17 seconds excluding GCP refinement, and less than 1 minute with GCP extraction and refinement (3 GCP's). The Pass-II software, operating on an image of 10^6 pixels, requires 52 seconds for bilinear interpolation and 110 seconds if the TRW Cubic Convolution Process is selected. The Pass-II nearest-neighbor interpolation requires about 30 seconds/ 10^6 pixels.

Cursory extrapolation of these numbers to a minicomputer indicate that Pass-I should execute as fast or faster than the CDC FORTRAN implementation. The bulk of the computing load, however, is in the Pass-II process; minicomputer throughput for the bilinear software is estimated at less than 5 minutes/MSS image, while the TRW Cubic Convolution Process is estimated to require less than 10 minutes/MSS image.

Table 2-5. Module Throughput

ELEMENT	CPU TIME (sec)
PASS-I	
1. Attitude/ephemeris time-series fittings; distortion coefficient calculation	16.1
2. GCP extraction)per GCP	14.2
3. Kalman filter refinement (15 GCP)	4.1
PASS-II (10^6 Pixels)	
1. Nearest-neighbor	30
2. Bilinear	52
3. TRW Cubic Convolution	110

3

RBV DATA PROCESSING

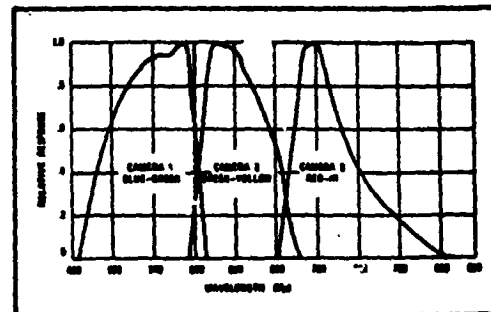
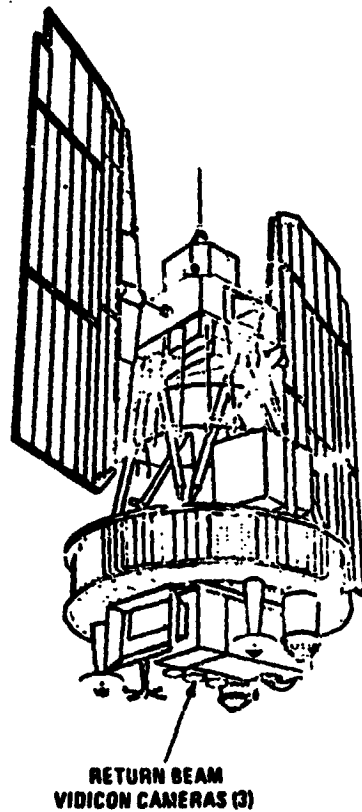
3.1 INTRODUCTION

The Return Beam Vidicon (RBV) camera subsystem contains three individual cameras that operate in different nominal spectral bands. The measured spectral response of the three cameras is shown in Figure 3.1. Each camera contains an optical lens, a shutter, the RBV sensor, a thermoelectric cooler, deflection and focus coils, erase lamps and the sensor electronics. The cameras are similar except for the spectral filters contained in the lens assemblies to provide separate spectral viewing regions. The sensor electronics contain the logic circuits to program and coordinate the operation of the three cameras as a complete integrated system and provide the interface with the other spacecraft subsystems.

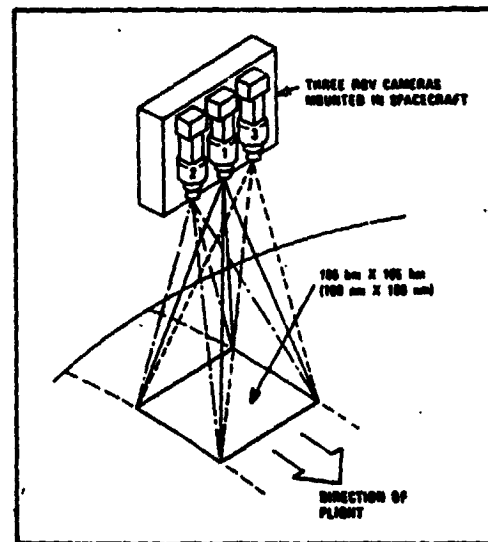
The three RBV cameras are aligned in the spacecraft to view the same nominal 185 kilometers (100 nautical mile) square ground scene as depicted in Figure 3.1. When the cameras are shuttered, the images are stored on the RBV photosensitive surfaces, then scanned to produce video outputs. The three cameras are scanned in sequence during the last 10.5 seconds of the basic 25 second picture time cycle. The video from each is serially combined with injected horizontal and vertical sync. The readout sequence is camera 3, then camera 2, then camera 1.

The digital reduction of the RBV data involves the following processing:

- Search for and measure positions of reseau
- Perform a polynomial fit to measured reseau positions and extrapolate positions of lost reseau
- Search for ground control points and measure displacements from nominal positions



Spectral Response, RBV Camera System



RBV Scanning Pattern

SOURCE: REFERENCE 2

Figure 3.1. RBV Subsystem

- Compute grid of pseudo-reseaux positions at 113 pixel intervals based on bi-quadratic coefficients determined from displacements of 9 nearby reseaux, and ground control point displacements
- Compute piecewise bilinear distortion coefficients for intervals between pseudo-reseaux
- Resample entire scene on a regular output grid (see Section 2.3.5 for discussion of resampling techniques used in this study).

Because of the large amount of digital data in each scene, those processes involving comparisons or interpolation at individual pixel levels have been analyzed and coded for high efficiency. The search for the reseaux, the search for the ground control points, and the final resampling require pixel by pixel treatment of large segments of the data. As a result, sophisticated analytic techniques have been used to reduce the number of pixels handled (i.e., the searching is made efficient by using as much information and insight as possible).

3.2 APPROACH

3.2.1 Reseau Extraction

The reseau marks for an RBV frame are placed in a 9 x 9 array on the RBV tube so as to be superimposed on the RBV image. They are placed with an accuracy of 3 micrometers or 1/4 pixel accuracy. The RBV faceplate reseaux have three possible locations: (1) intended, (2) nominal, (3) measured (found). The intended locations of reseaux lie on a regular grid and represent the desired positions. Due to imperfections in the process by which they are created on the faceplate, their actual locations are slightly different from the intended locations. Calibration data supplied by NASA corresponds to the nominal reseau positions. The locations actually found as a result of Pass 1 processing are denoted as measured positions. In addition, reference locations in the output corrected image correspond to regular grid locations (very close to the intended grid positions) with respect to which the Pass 2 coefficients are defined.

The nominal displacement in each coordinate is less than 1 pixel; the measured displacement is normally less than 3% or 120 pixels. The dimensions of the entire RBV frame is 4125 lines with 4608 pixels per

line in bulk format.

For each reseau a 240 x 240 pixel neighborhood is called from disk storage, with the intended reseau location at the center of the neighborhood. In searching for the reseau, a neighborhood is divided into blocks of 15 x 15 pixels. Excluding a band 15 pixels wide at the edges of the neighborhood, each block is searched to see if it contains the center of the reseau. Because a reseau is 32 pixels wide, 32 pixels high, and 4 pixels across each arm, the center must be at least 16 pixels from the edge of the neighborhood for the whole reseau to be contained in the neighborhood. Therefore, the center cannot be in the outer 15 pixels, and only the inner blocks of the neighborhood need be searched for the reseau center.

The order in which the blocks are searched is determined first by the block in which the last reseau was found. If this block and those immediately adjacent to it fail to contain the reseau center, then a spiral pattern of blocks is searched, moving outward from the intended reseau location (skipping those searched in the first try near the block predicted from the previous RBV image). Before a block is searched for the reseau center, the border of the block is examined to see if any edge of the block fails to have a black pixel (checking every other pixel). If the center of the reseau is inside the block, then at least two adjacent pixels on each edge must be black because one of the reseau arms will cross it. The block is not searched if it cannot meet this test.

To search a block for the reseau center, a check is made of every second pixel in alternate rows from the top to the bottom of the block. When a pixel is found to be black, then pixels at locations ± 12 and ± 6 in both coordinates are also checked to see if they are black. (Note that only the center pixel is required to be in the block being searched. Some of the surrounding pixels tested will be outside the block, but still inside the neighborhood. Hence, their intensities will be available.)

After a candidate center has passed the search criteria described, a shadow casting routine is used to determine whether the real reseau center is within ± 2 pixels of the candidate center. Only a 27 x 27 pixel reseau is sought (that is, the sums for the shadow casting include 27 pixels).

since the outer pixels may be lost in distortions, and so that the reseau will be detected even if the candidate center is displaced as much as two pixels from the true center. A set of 13 line sums is made in each coordinate, centered about the candidate center. Seven sums are considered in the search for a minimum intensity, while the outer 6 sums are available for information on the background. If one of the sums in each coordinate is below an input threshold ($27 \times IT$) and if all of the sums three pixels away from it are at least an input increment (IDEL) greater, the reseau is found. The threshold increment $ITINC (=7)$ for $IT (=3)$ is cumulated until the sum of $IT+ITINC$'s exceeds $ITOP$ if a reseau does not pass this test. No more than 3 iterations ($ITOP=17$) were required in this study, and no false alarms were encountered.

The precise center location is then found by a three point interpolation around the minimum sum in each coordinate. Finally, the nominal displacement is subtracted from the measured displacement to obtain the distortion correction to be applied at the intended reseau location. The known reseau displacements are used to find the coefficients \hat{a} , \hat{b} , for the global third order polynomial:

$$\begin{aligned} \delta x &= \sum_{i=0}^3 \sum_{j=0}^{3-i} a_{ij} x^i y^j & \hat{a} &= (A^T A)^{-1} A^T \delta x \\ \delta y &= \sum_{i=0}^3 \sum_{j=0}^{3-i} b_{ij} x^i y^j & \hat{b} &= (A^T A)^{-1} A^T \delta y \end{aligned}$$

All reseau displacements are then predicted. The known reseau displacements are tested to see whether they differ an unacceptable amount (TH) from their predicted displacements. Those rejected, and those not found originally are assigned the predicted displacement value.

An option permits the recomputation of the predicted displacements with the rejected reseaux eliminated from the coefficient determination (an iteration). In this case, any additional reseaux that fail to be close enough to the recomputed predicted value are simply assigned their

predicted value.

3.2.2 Ground Truth Computation for Attitude and Ephemeris Error

Because of vehicle attitude and position uncertainties, ground control points are located. Their displacements ($\delta x_i, \delta y_i, i=1, N$) on the RBV image, are used to solve for the corrections to vehicle position and attitude:

$$B = \begin{bmatrix} \delta x_0 \\ \delta y_0 \\ \theta_R \\ \theta_P \\ \theta_Y \\ \delta H \end{bmatrix}$$

where $\delta x_0, \delta y_0, \delta H$ are position errors along-track, cross-track, and in attitude, and $\theta_R, \theta_P, \theta_Y$ are departures from nadir in the roll, pitch, yaw coordinates. Inputs estimates B_0 for B , and its inverse covariance matrix, SI , obtained from the ephemeris tape data, are combined with the solution from ground control displacements to yield a best estimate, \hat{B} of B :

$$\hat{B} = (M^T M + SI)^{-1} (M^T \delta W + SI \cdot B_0),$$

where

$$\delta W = \begin{bmatrix} \delta x_1 \\ \vdots \\ \delta x_W \\ \delta y_1 \\ \vdots \\ \delta y_W \end{bmatrix}$$

and where the rows of M are:

$$M_i = [1, 0, (Hx \frac{y^2}{H}, \frac{xu}{H}, xH, \frac{y}{H})]$$

for $1 \leq i \leq n$, and for $n+1 \leq j \leq 2n$

$$M_j = [0, 1, (Hx \frac{y^2}{H}, \frac{xu}{H}, xH, \frac{y}{H})]$$

The search for the ground control points requires a fast and simple means to recognize known ground features. The method of Reference (3) has been coded, with modification, to allow the inclusion of a set of priority pixel points for comparison before the comparison of random points. A window of dimension 32 x 32 pixels about the desired ground control point, is assumed for the given site. As many as 50 pixels within the window may be entered as special priority pixels for scene recognition. A neighborhood of 120 x 120 pixels off the RBV image is taken from disk storage to compare with the window. By knowing the reseau displacement for a nearby reseau, the displacement of the ground control point on the RBV image from its nominal position due to distortions can be predicted, and the residue of attitude displacement and ephemeris error can be limited to ± 60 pixels). A larger block of data is stored in the initial stripping of data off the bulk tapes (300 x 300 pixels), and the predicted displacement used to enter the larger block to obtain the 120 x 120 pixel neighborhood.

In brief, the technique used to recognize the ground control point involves repeated comparisons of the window with subsets of the neighborhood. Each comparison is made until the summed residuals between the compared pixels in the window and the subset exceed a threshold. The number of pixels compared before reaching the threshold is used as a measure of the goodness of fit between the two scenes. The threshold is an increasing one, based on the expected residuals due to noise. Both the window intensities and the subset intensities are normalized before differencing to obtain the residuals. The order in which pixels are compared is as follows: First the priority pixels are compared, and then a random order of points established one for all subset comparisons is

followed. The randomness assures that a variety of information is used to measure the fit.

The summation of normalized residuals is as follows:

$$\sum \epsilon_i = \sum (S_i - \hat{S} - W_i - \hat{W})$$

where S_i is the intensity for pixel i in the subset, W_i is the intensity for pixel i in the window, \hat{S} is the mean intensity for the subset, and \hat{W} is the mean intensity for the window. Subroutine NORMAL computes \hat{A} and \hat{W} . Subroutine RAND assigns the order of i . Subroutine SURFAC performs the comparisons and keeps track of the subset having the largest number of comparisons before exceeding the threshold. The threshold is based on the results of Reference (2) and may be written as:

$$JT = 9 \times \text{NOISE} + \sum_i \text{NOISE}$$

and is easily computed by a single add for each comparison. NOISE is the mean of the image noise.

The normalization process requires that \hat{S} be recomputed for each subset. This is accomplished by incrementing the previous value to avoid $(32)^2$ additions.

3.2.3 Pseudo-Reseau Grid Generation

In a study performed by TRW prior to this contract, modeling error analyses were performed for piecewise biquadratic and piecewise bilinear distortion models, and global third order and biquadratic interpolation was found to be most efficient and accurate for the RBV problem. For the error resulting from the interpolation statistics themselves, due to spatially-uncorrelated distortions and reseau measurement errors, the piecewise biquadratic method results in a ratio of error in interpolation to error

in reseau position, σ/σ_R , of 1 for points internal to the grid and 5 at the corners. Figure 3.2 shows graphically how the ratio varies over a scene. For example, if the error in measuring reseau is 1 pixel, the internal error for the interpolation would be 1 pixel, and the error at the edges and corners of the scene would reach 5 pixels, resulting from the piecewise biquadratic distortion model used to obtain pseudo-reseau positions. (This biquadratic model is the major error source). The sensitivity of the piecewise biquadratic to modeling errors for 1% first-order pincushion, 0.2% second-order pincushion, and 0.5 pixel 1-sigma random distortion (a bad set of distortions) will result in errors of:

Up to 1 pixel at corners of scene

Up to 1/6 pixel internal to scene

1/4 pixel RMS error over all of the scene

The other methods tested produced errors as much as 10 times larger.

To utilize bilinear interpolation of distortions to compute the geocentric correction for each pixel, a pseudo-reseau grid is computed using a global biquadratic polynomial. The polynomial predicts the displacement for pseudo-reseaux placed every 113 pixels between the reseau, which are at 452 pixel intervals. At the outer edges of the reseau grid, two rows of pseudo-reseaux are extrapolated. Nine reseau points are used at a time to obtain the pseudo-reseaux contained between them and on the outer borders. Figure 3.3 shows the 16 reseau subregions of 9 reseau each used to compute pseudo-reseaux. The original reseau points are included in the 37 x 37 matrix of pseudo-reseau points prepared for the final bilinear interpolation.

The coefficients for the global biquadratic fit are contained in:

$$\delta \bar{x} = \sum_{i=0}^2 \sum_{j=0}^2 a_{ij} x^i y^j = \hat{a} A$$

and are computed from

$$\hat{a} = A^{-1} \delta x$$

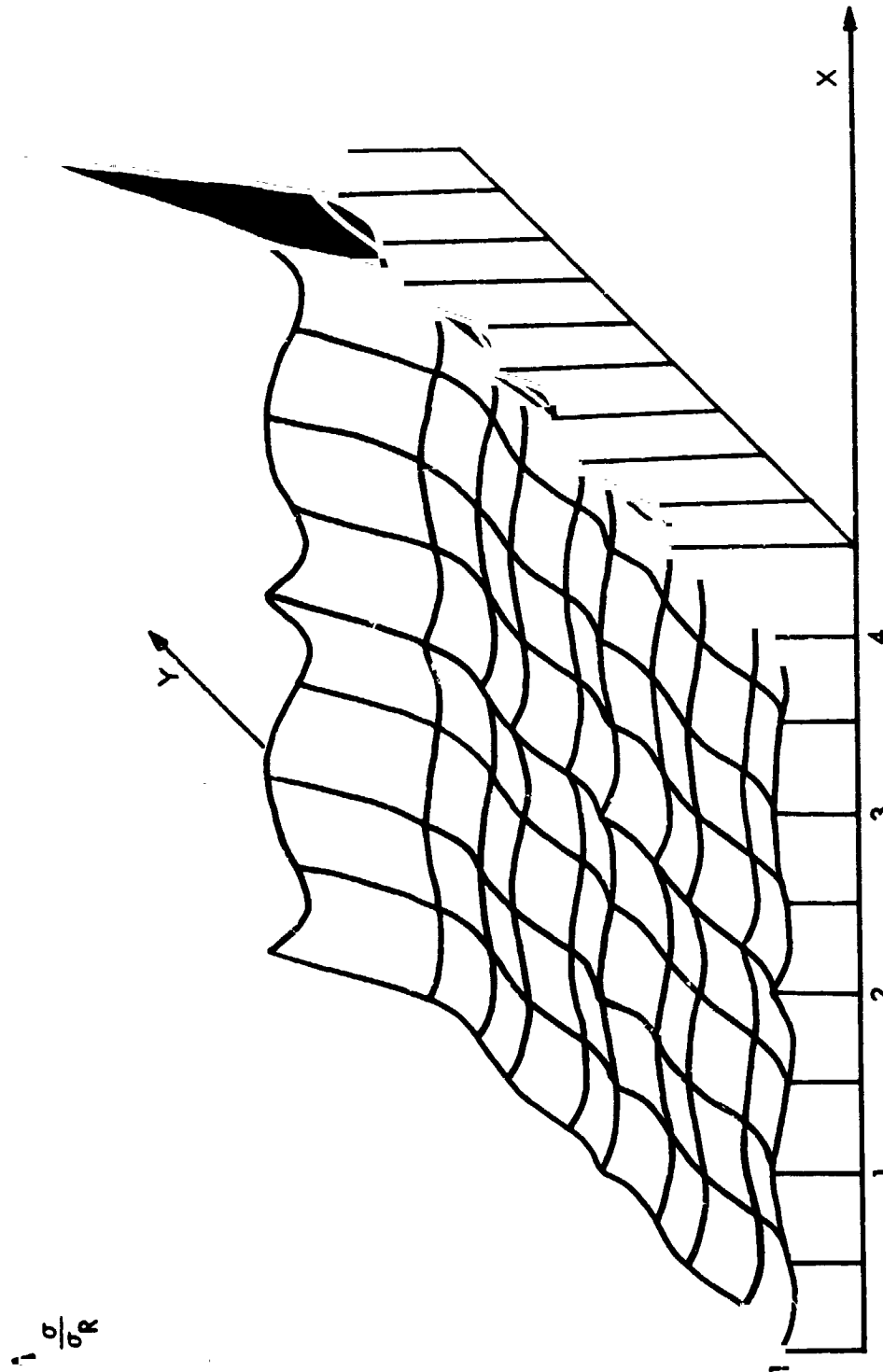


Figure 3.2. The Statistical Function (σ/σ_R) for the Piecewise Biquadratic Approach

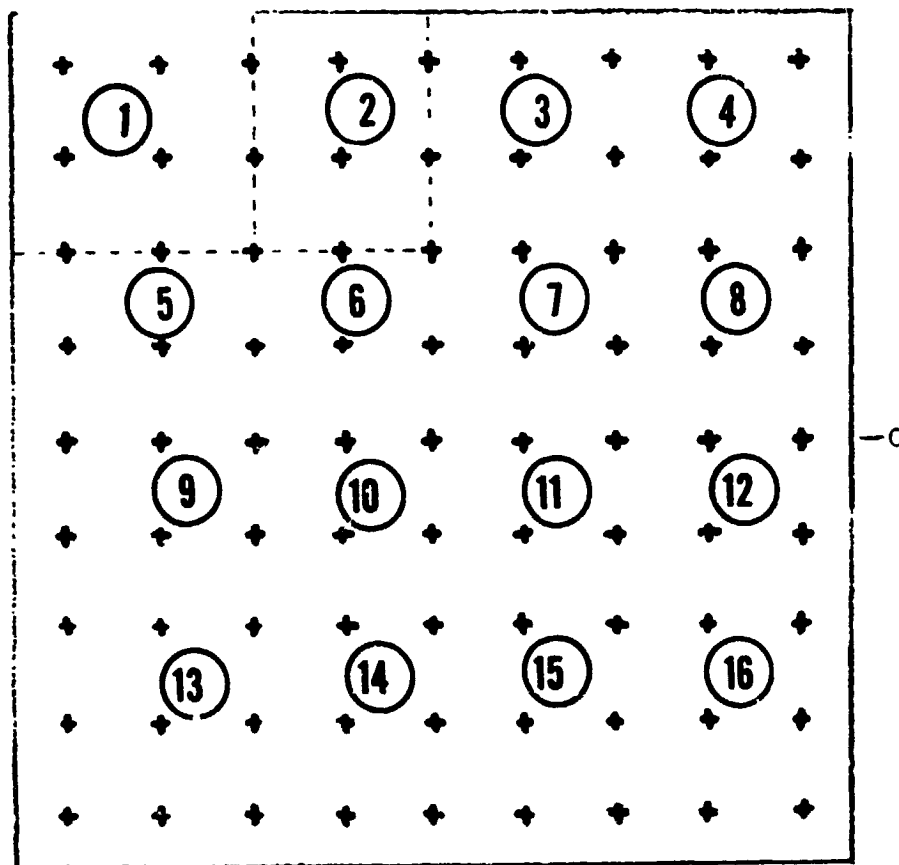


Figure 3.3. Reseau Subregions

Intended locations of reseaux define border of regions, with 9 reseaux in or on the border of each region for use in biquadratic interpolation within the region. The measured reseau displacement minus the nominal displacement is assumed to apply at the intended reseau location. For the ij^{th} reseau, the intended location is

$$M_x = 452i - 2260$$

$$M_y = 452j - 2260$$

where the A matrix has rows

$$[1, x, x^2, y, xy, x^2y, y^2, xy^2, x^2y^2]$$

one row for each of the nine reseau locations, and \hat{a} is a vector containing the nine coefficients, a_{ij} , of these terms. The quantity $\delta\bar{x}$ is the displacement in x at the reseau point. A similar equation yields the y displacement coefficients:

$$\delta\bar{y} = \sum_{i=0}^2 \sum_{j=0}^2 b_{ij} x^i y^j$$

$$\hat{b} = A^{-1} \delta\bar{y}$$

These \hat{a} and \hat{b} coefficients are computed by the routine entitled SUBREG. The BIQUAD routine uses them to compute the displacements for all the subreseau points. Corrections for earth curvature and satellite attitude are supplied to SUBREG by the INCORP routine. By applying them at this level, it is possible to use an adequate second order model without the high cost computationally of a later correction to the 4096^2 pixel points. Where ground control points are used, the GTRUTH subroutine provides an attitude correction vector to INCORP resulting from a combination of attitude and ephemeris predicted data with the ground truth observations. When the ground control points are not found or are not available for that RBV frame, GTRUTH provides the attitude correction vector based on attitude instrumentation and ephemeris data only.

3.2.4 Bilinear Coefficient

Using the displacements computed for each subreseau point, subroutine LINCO computes the 8 coefficients (4 for x and 4 for y interpolation) required for the bilinear distortion model for pseudo reseau points.

The coefficients are defined by:

$$\begin{bmatrix} \delta x_1 \\ \delta x_2 \\ \delta x_3 \\ \delta x_4 \end{bmatrix} = \begin{bmatrix} 1 & x_1 & x_1 y_1 & y_1 \\ 1 & x_2 & x_2 y_2 & y_2 \\ 1 & x_3 & x_3 y_3 & y_3 \\ 1 & x_4 & x_4 y_4 & y_4 \end{bmatrix} \begin{bmatrix} A_x \\ B_x \\ C_x \\ D_x \end{bmatrix}$$

The above may be simplified by noting that (x_1, y_1) , (x_2, y_2) , (x_3, y_3) , and (x_4, y_4) are corners of a square with sides of 113. ($x_3 = x_1$, $y_2 = y_1$, $x_2 = x_1 + 113$, etc.). An analytic inversion of this set of equations for the coefficients:

$$C_x = \frac{1}{(113)^2} (\delta x_4 + \delta x_1 - \delta x_3 - \delta x_2)$$

$$B_x = \frac{1}{113} (\delta x_2 - \delta x_1) - C_x y_1$$

$$D_x = \frac{1}{113} (\delta x_3 - \delta x_1) - C_x x_1$$

$$A_x = x_1 - B_x x_1 - C_x x_1 y_1 - D_x y_1$$

For y : C_y , B_y , D_y , A_y are obtained by analogous expressions with δx_i replaced by δy_i .

These computations are made in subroutine LINCO.

3.3 RBV DATA PROCESSING RESULTS

Due to the shutdown of the RBV subsystem shortly after ERTS-1 launch, processing priority was shifted to MSS data although considerable progress had been made during the pre-launch study phase to modify TRW algorithms to accommodate the RBV data. The software was found to be nearly adequate the first time it was utilized and only minor modification was required.

With respect to reseau extraction, no measurable position errors were found, and no false detections were encountered. Average CPU time for reseau extraction was found to be 0.415 seconds, including cases of threshold iteration (no more than two such iterations were required for any reseau).

GCP extraction software performance has already been discussed in Section 2. Throughput performance for the RBV software using a CDC 6400 computer is summarized in Table 3-1.

Table 3-1. Module Throughput

<u>Element</u>	<u>CPU Time</u>
PASS I	
1. Reseaux Extraction (81 Reseaux)	33.6 sec
2. Distortion Coefficient Calculation	10.1 sec
PASS II (Per Band)	
Nearest Neighbor	8.4 min
Bilinear	14.6 min
TRW Cubic Convolution	30.8 min

The image 1002-18134-1 is typical of RBV processing results. Figure 3.4 illustrates the NASA system corrected image. Figure 3.5 shows a detail 960 pixels by 1130 lines reproduced on a line printer from the bulk CCTs. Figure 3.6 shows the subregion following precision digital processing by means of the methods described earlier in this section. Figure 3.7 shows the corresponding detail from the NASA system corrected image. Section 4 contains results for various resampling comparisons and analyses.

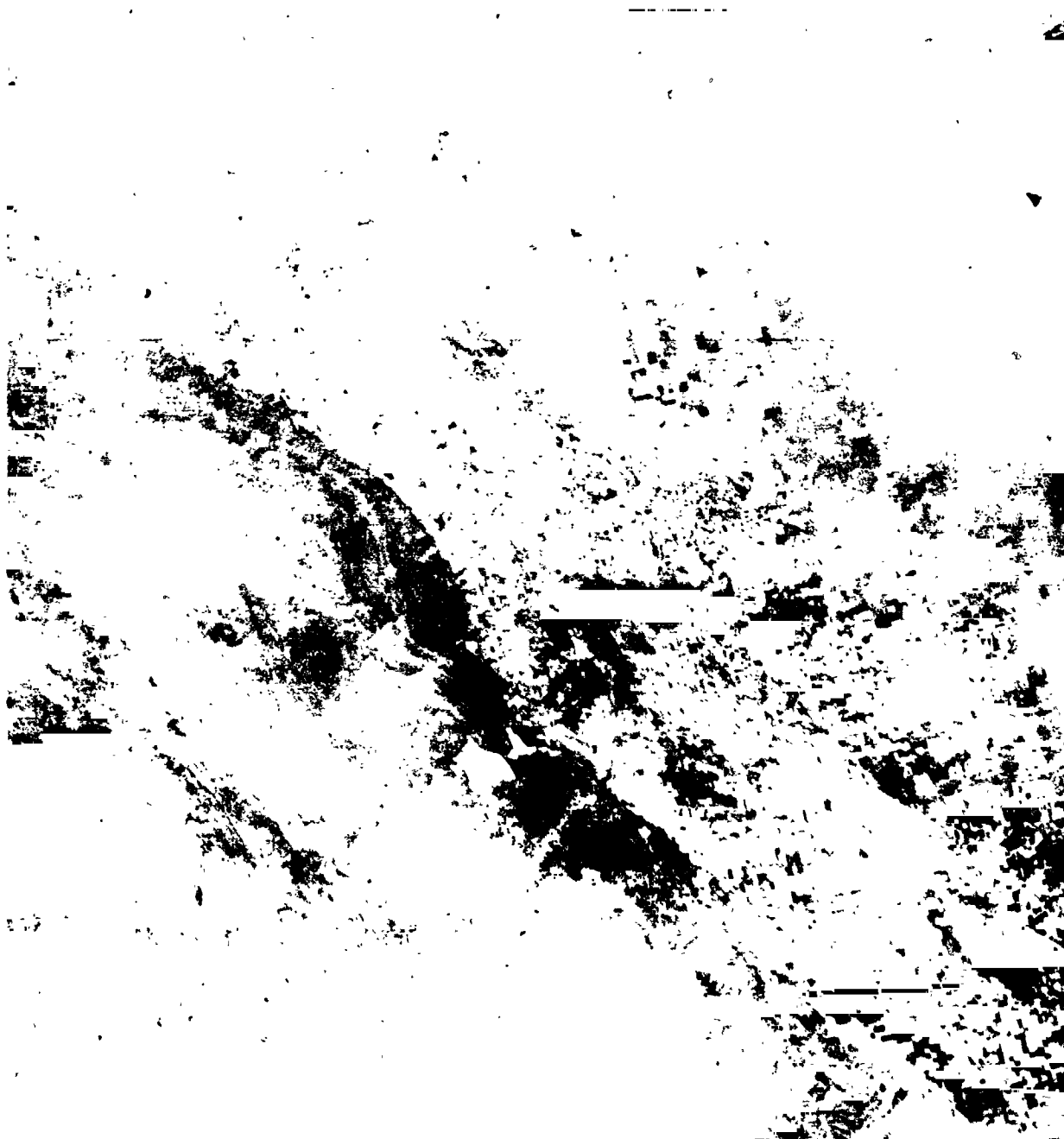


Figure 3.4 System Corrected RBV Image 1002-18134-1



Figure 3.5. Detail from map 1002-18134-1 Bulk Data

This figure is a photo reduction of line printer outputs. The hash marks running vertically represent position indicators; they are not in the processed data.

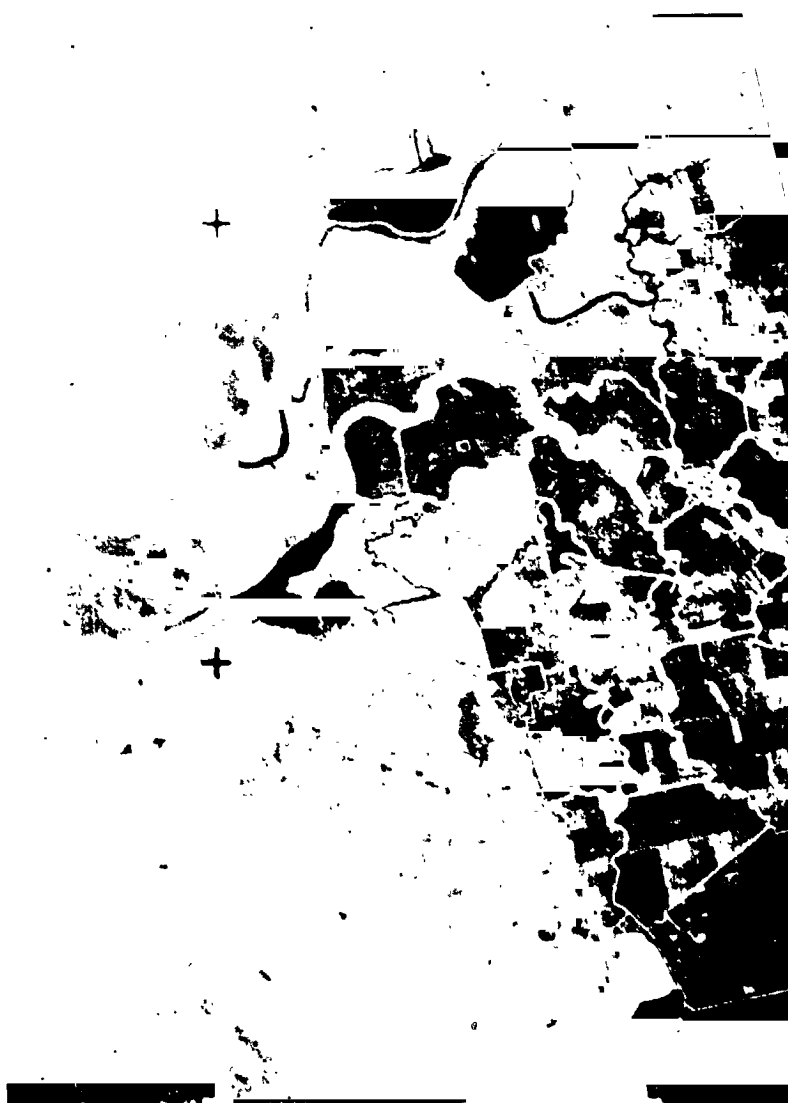


Figure 3.6 Detail from TRW Precision Product for Image 1002-18134-1



Figure 3.7. Detail for NASA System Corrected Product for Image 1002-18134-1

4

RESAMPLING COMPARISONS

A significant problem in correcting bulk-image data is the generation of image data for pixel locations other than the sampled locations. There are two ways to correct image data after determining the necessary geometric and radiometric corrections: (1) Move the sampled pixels around, (e.g., EBR beam position modulation); (2) interpolate the pixel values around the desired location ("resampling").

TRW has employed the latter process, which in contrast to the former produces a digital data stream as the output product. The input to the resampling process, which is the second pass process indicated in Figure 1.2, consists of the file of distortion coefficients for 64 piecewise bilinear distortion regions and the reformatted bulk image data. Conceptually, the Pass-II process consists of reconstructing in its entirety the corrected (rectified) image and then sampling its intensity values at predesignated positions (lines/pixels) within the bulk image. It should be clearly understood that at no time is the input image data physically distorted. The power of the resampling method becomes clear when it is realized that complete flexibility is afforded in the matter of pixel spacings and line spacings (independently), thus making possible the custom tailoring of the corrected image to any application and/or hardware constraints.

The resampling method is implemented by means of an interpolation process. One-dimensional interpolation of band-limited digital data is of the form:

$$I(x_i) = \sum_{u_k} I(u_k) f(x_i - u_k)$$

wherein $f(x)$ is the interpolation kernel, x_i is the argument (pixel location) chosen for the resampled function I , and the set of u_k is the set of arguments of the available digital data $I(u_k)$, that is, the bulk data values. Three kernels, corresponding to: (a) nearest-neighbor interpola-

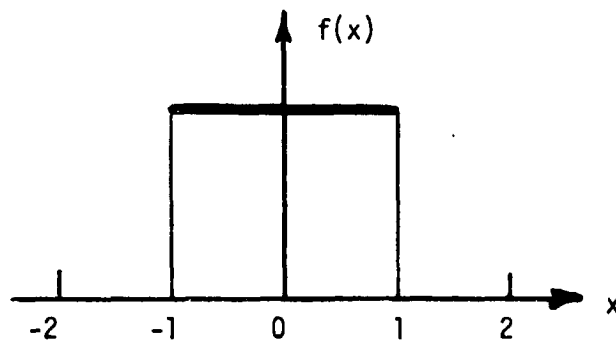
tion; (b) bilinear interpolation; and (c) TRW's Cubic Convolution Process, are shown in Figure 4.1 for one dimension. In the ideal band-limited case $f(x)$ is of the form $\sin x/x$, which TRW has approximated by the cubic spline function of Figure 4.1-c.

Nearest-neighbor interpolation involves choosing the value of the pixel closest to the desired pixel location as the interpolated value, as shown for one dimension in Figure 4.2. Only one pixel value of the bulk image is required for each interpolated value, and only original values are used. The algorithm is thus very fast. Note however that errors accumulate in finite ($\pm 1/2$ pixel) increments and thus will result in 1 pixel offsets throughout the corrected image.

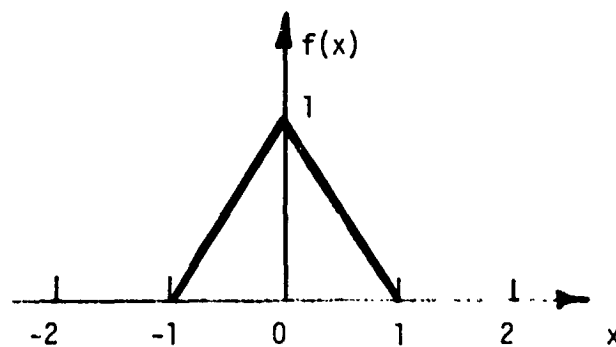
Bilinear interpolation, also shown for one dimension in Figure 4.2, utilizes a bilinear combination of the four closest pixel values to produce a new, interpolated pixel value. The smoothing effects of bilinear interpolation preclude the one pixel offsets characteristic of nearest-neighbor interpolation. On the other hand, this smoothing effect causes some image degradation in the form of edge smoothing and loss of maxima/minima fidelity. Also, the algorithm is inherently slower, inasmuch as a new pixel value must be computed from four other values.

In contrast to nearest-neighbor and bilinear interpolation, TRW's Cubic Convolution Process requires the values in a grid of 4 pixels x 4 lines about the point at which the interpolated value is desired. Thus, both slope and value continuity properties of the function to be re-sampled are preserved (as expected on the basis of its approximation to ideal $\sin x/x$ resampling). As a consequence, high resolution with minimum distortion results, with some penalty in CPU time compared to bilinear interpolation. It will be seen, however, that reasonable CPU times have been attained by TRW.

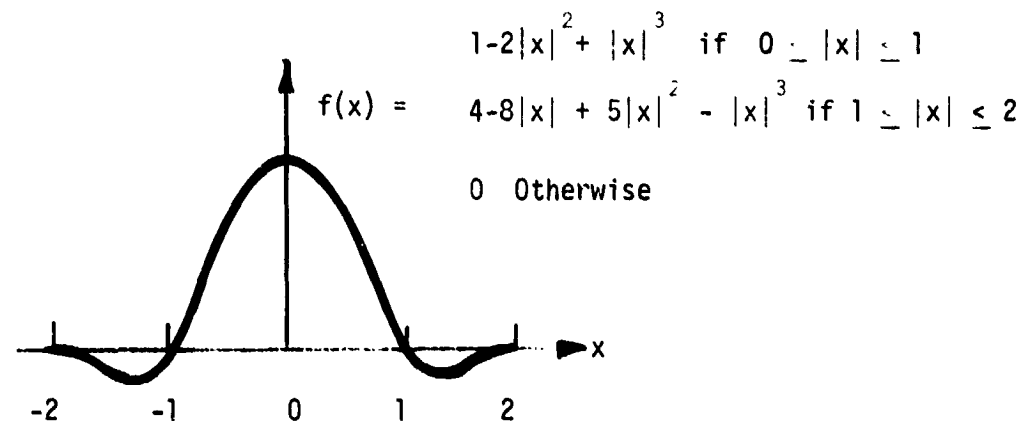
A comparison of performance is given in the error histograms of Figure 4.3. A reference image was generated by 900 point $\sin x/x$ and differenced pixel by pixel with the same image processed by 100 point $\sin x/x$, 16 point TRW Cubic Convolution, 4 point bilinear interpolation and 1 point nearest-neighbor interpolation. The error histograms shown in the figure indicate the clear superiority of TRW Cubic Convolution,



(a)

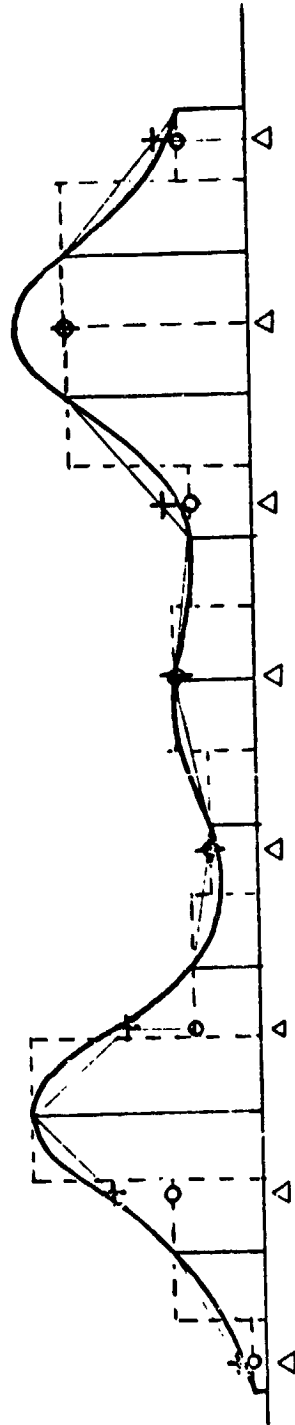


(b)



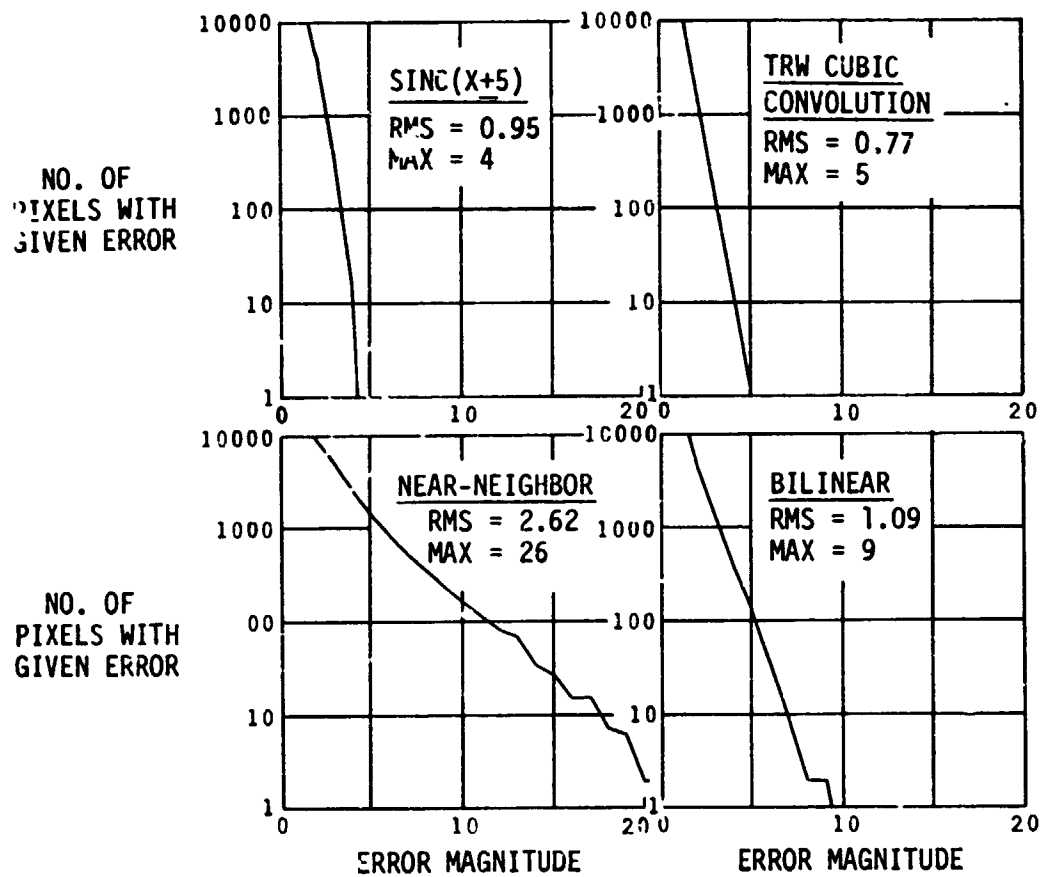
(c)

Figure 4.1. Three Interpolation Kernels. The three kernels correspond to (a) nearest-neighbor interpolation, (b) bilinear interpolation, and (c) TRW's Cubic Convolution Process.



Δ - OUTPUT SAMPLE TIMES
O - NEAREST NEIGHBOR SAMPLES
+ - BILINEAR INTERPOLATION SAMPLES

Figure 4.2. Nearest-Neighbor and Bilinear Interpolation



(INTENSITY RANGE IS 0 ~ 63)

Figure 4.3. Resampling Errors

which generated only one pixel (out of 49,600) with an error greater than $k00 \text{ point } \sin x/x$. TRW's Cubic Convolution Process gave the lowest rms error of the four considered.

Examples of imagery produced by the nearest-neighbor, bilinear and TRW Cubic Convolution Process are shown in Figure 4.4: the bulk image in the upper left, and the processed image using nearest-neighbor interpolation (upper right), bilinear interpolation (lower right), and TRW's Cubic Convolution Process (lower left). Note the many one pixel image discontinuities characteristic of nearest-neighbor interpolation, particularly evident for the road intersection in the upper left corner of the processed image. Bilinear interpolation, on the other hand, eliminates these discontinuities, at the expense of image resolution. Finally, the image processed by the Cubic Convolution Process shows none of the nearest-neighbor image discontinuities, and no loss of resolution. Figures 4.5 and 4.6 more clearly show the differences between nearest-neighbor and the TRW Cubic Convolution Process, respectively, reproduced by a filmwriter.

Spatial frequency analyses based upon the power density spectra for processed ERTS data have also been performed. Figure 4.7 was chosen as a typical image detail (scene 1062-15190-5), 100 lines x 128 pixels in the corrected image. This detail shows the intersection of I83 (Jones Falls Expressway) and I695 (Baltimore Beltway), and is reproduced from line printer output.* Using TRW's Fast Fourier Transform Process, line power density spectra were obtained for the detail and then averaged (spectral component by spectral component) over all 100 lines. This was done in turn for nearest-neighbor, bilinear and TRW's Cubic Convolution Process. To eliminate leakage due to a large dc component, the mean was removed, padding zeros were added to the data and a Hamming Window (cosine taper at the image edges) was employed.

The results are plotted as a function of $|w|$ (rad/meter) in Figure 4.8. The low frequency contents of three resampled images are very

* A dot matrix 3 dots on a side permits use of 10 gray levels for each pixel.

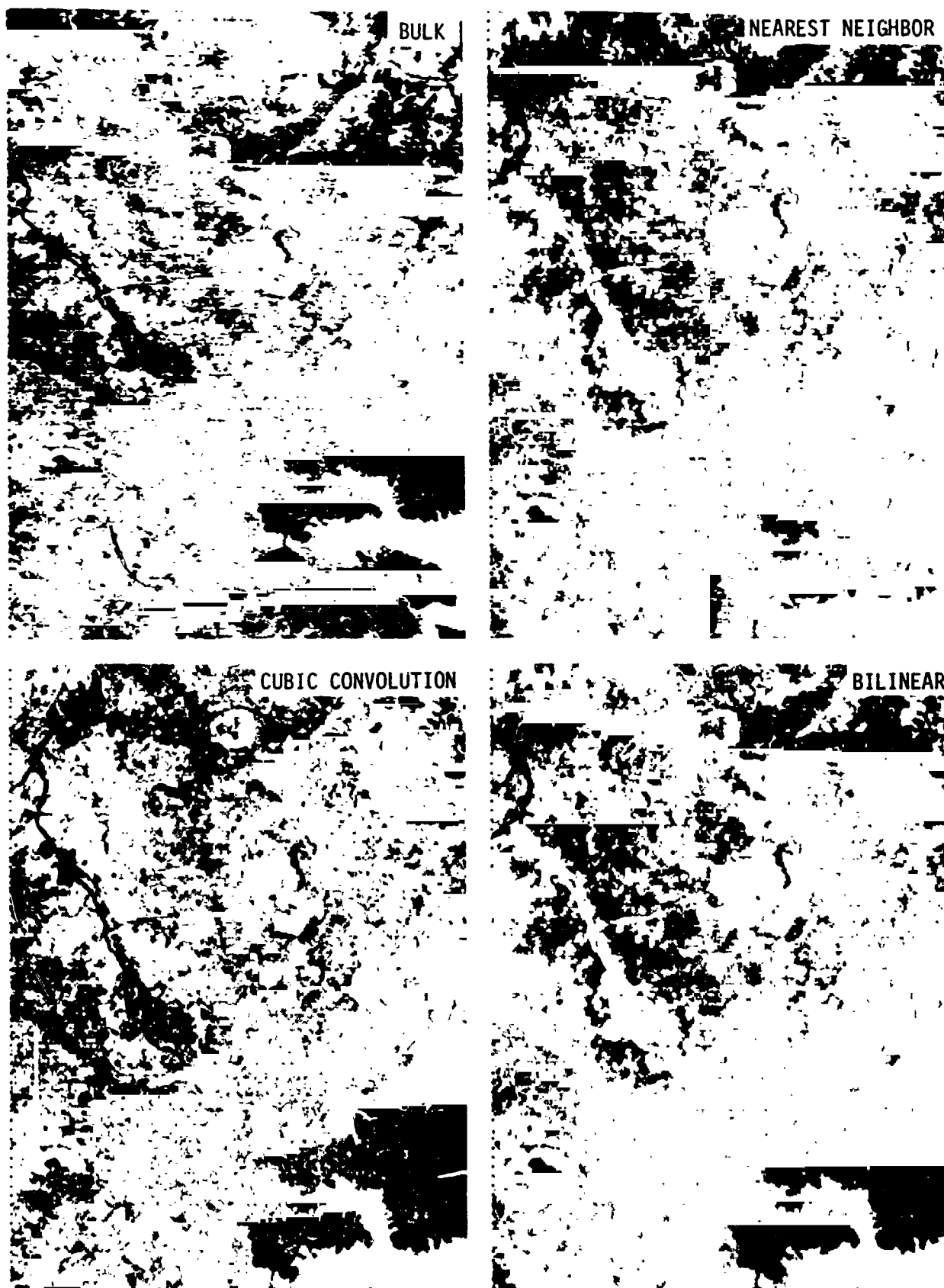


Figure 4.4. Corrected Image Detail for Three Interpolation Algorithms

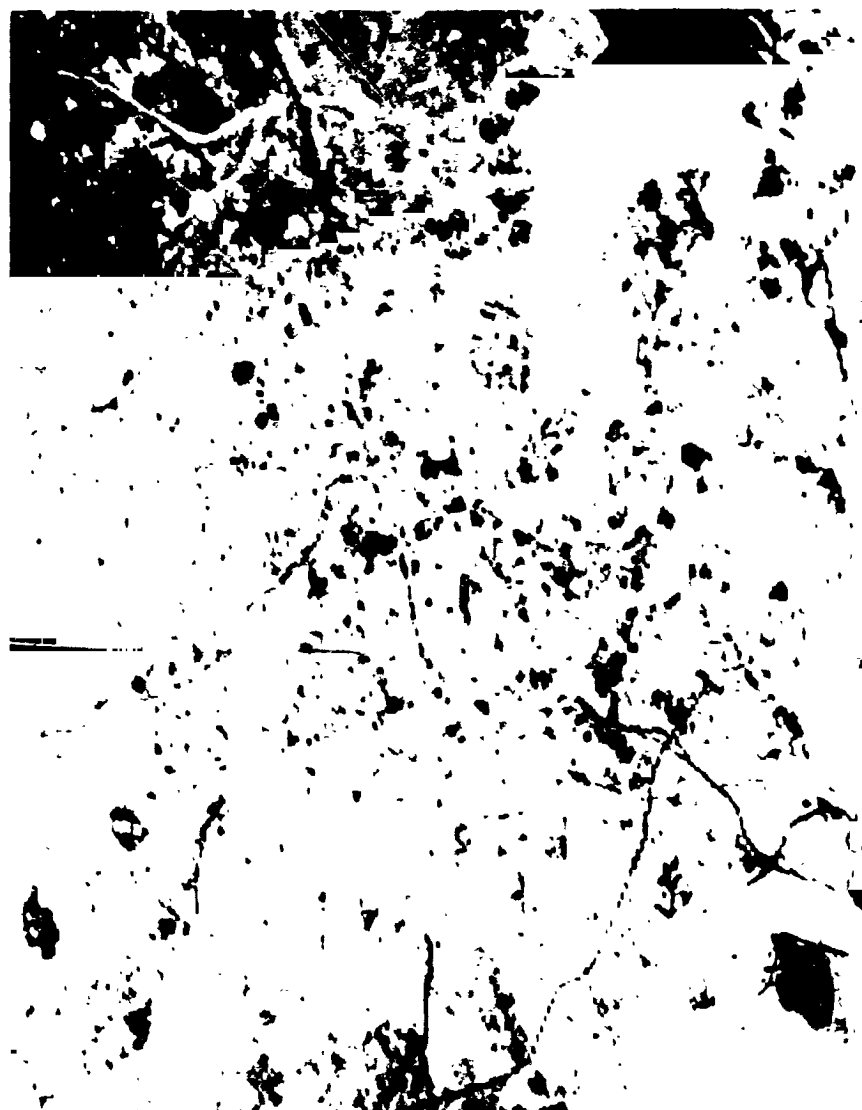


Figure 4.5. Nearest-Neighbor Processed Image Detail



Figure 4.6. TRW Cubic Convolution Processed Image Detail



Figure 4.7. Detail of Precision Processed 1062-15190-5
This line-printer output shows the Intersection of 183 and 1695,
resulting from TRW Cubic Convolution Processing.

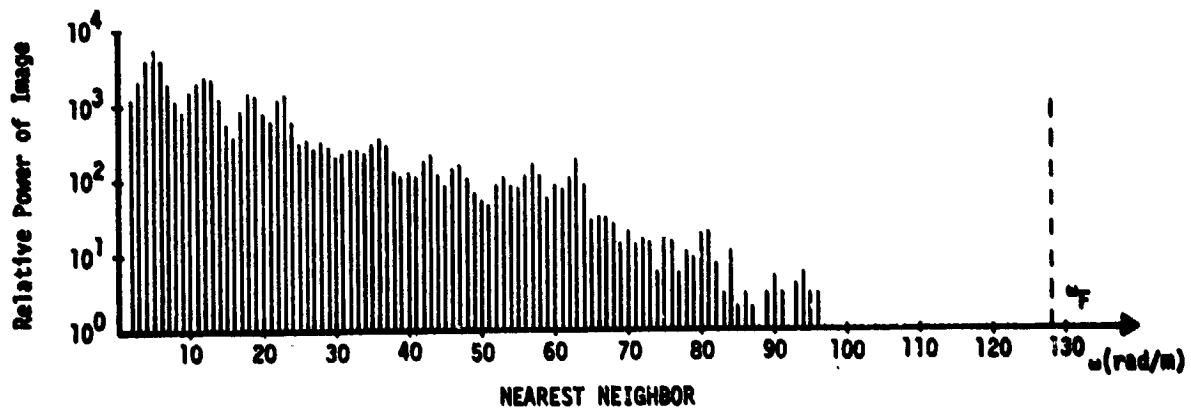
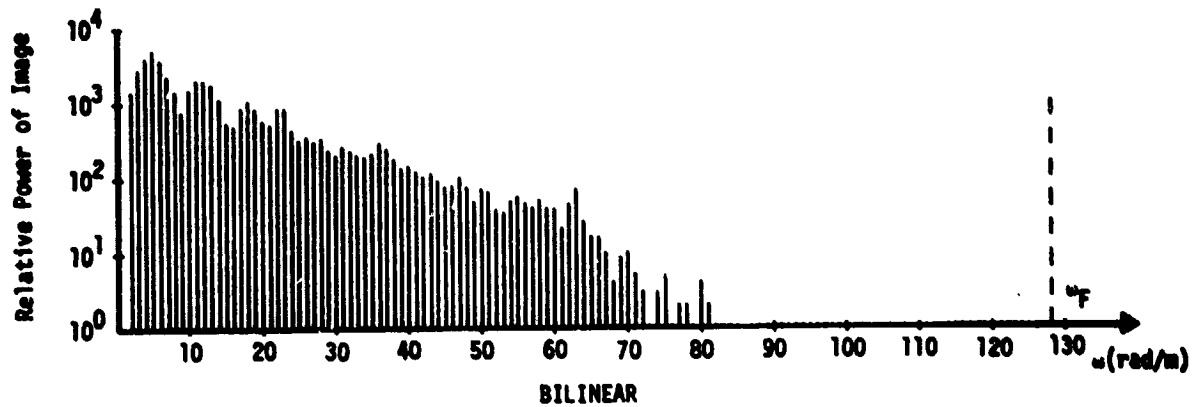
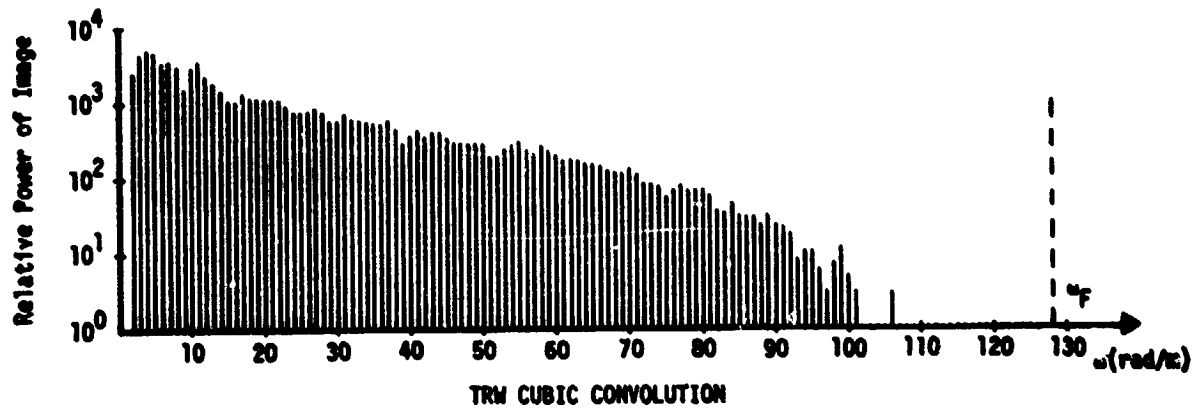


Figure 4.8. POWER SPECTRAL DENSITY : AVERAGED FOR 100 LINES

The folding frequency is denoted by ω_F , and the
frequency interval $\Delta\omega = \frac{2\pi}{256 \times 57}$ radian/meter

nearly the same. However, that corresponding to the TRW Cubic Convolution Process contains more high frequency components than bilinear resampled images. This is an expected result due to the smoothing nature of bilinear interpolation. The nearest-neighbor processed image is not greatly different from the TRW Cubic Convolution (bear in mind, the small relative power at the highest spatial frequencies).

Another way of comparing the three resampling techniques is to generate three images shifted one-half pixel for the scene of Figure 4.9 (bulk data) by the use of nearest-neighbor, bilinear and TRW Cubic Convolution Process, respectively. The power density spectra of the three shifted images were computed by again averaging over 100 lines. Results, plotted in Figure 4.10, show that the power density spectrum of nearest-neighbor resampled images is indistinguishable from the power spectrum of the original bulk image since a linear shift of half pixel by means of nearest-neighbor resampling should preserve the image samples and thus the statistics. The bilinear resampled image suffers the loss of high frequency components because of the smoothing effect of bilinear reconstruction. The power density spectrum corresponding to TRW's Cubic Convolution Process has essentially the same spatial frequency content as the nearest-neighbor resampled image; however, the high frequency components are not degraded as is the case for bilinear interpolation.

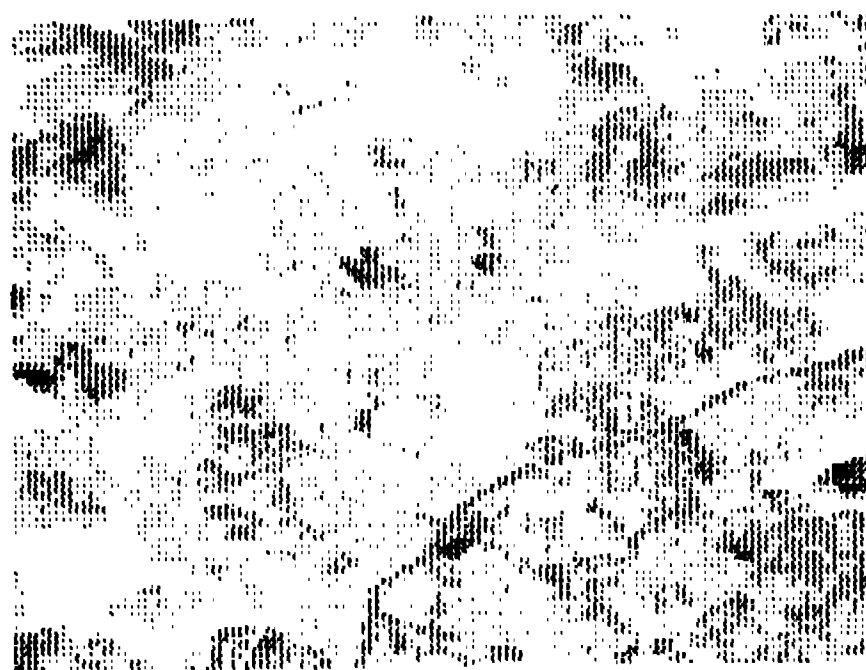


Figure 4.9. Second Detail of Precision Processed 1062-15190-5

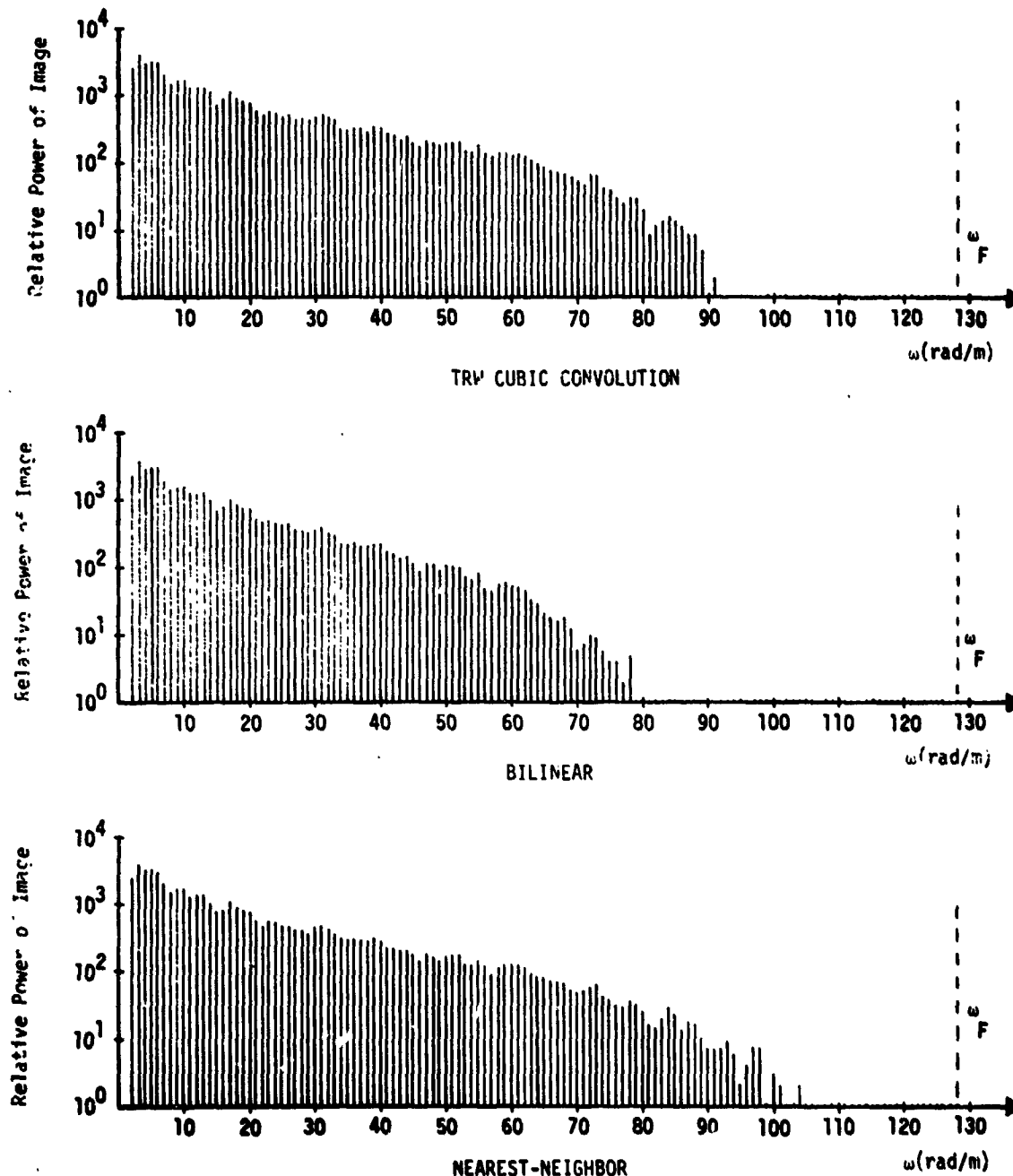


Figure 4.10. Power Spectral Density of Image Shifted one-half pixel: Averaged for 100 lines

The folding frequency is denoted by ω_F , and the frequency interval $\Delta\omega = \frac{2\pi}{256 \times 57}$ radian/meter

5

R E F E R E N C E S

- (1) TRW Proposal 24426, "Digital Correction and Information Extraction Techniques for ERTS Images," 31 January 1973.
- (2) NASA Document 71SD4249, "Data Users Handbook, ERTS Resources Technology Satellite."
- (3) IEEE Transactions on Computers, "A Class of Algorithms for Fast Digital Image Registration," D.I. Barnea, H.F. Silverman, Vol. C-12, No. 2, February 1972.
- (4) NASA Document X-563-73-206, "Generation and Physical Characteristics of the ERTS MSS System Corrected Computer Compatible Tapes," July 1973.
- (5) Paper I6 by S.S. Rifman, "Digital Rectification of ERTS Multispectral Imagery," NASA Document SP-327, Symposium on Significant Results Obtained from the Earth Resources Technology Satellite-1, Vol. I-Section B, March 5-9, 1973.
- (6) American Society of Photogrammetry, Symposium Proceedings, Management and Utilization of Remote Sensing Data, 1973, Paper by S.S. Rifman, "Evaluation of Digitally Corrected ERTS Imagery," October 29-November 1, 1973.
- (7) Paper I10 by J.E. Taber, "Evaluation of Digitally Corrected ERTS Images," Third ERTS Symposium, December 10-14, 1973, Sponsored by NASA/GSFC.
- (8) TRW Report 20634-6001-RU-00, "Evaluation of Digital Correction Techniques for ERTS Images," Interim Report for the Period September 1972 - February 1973, March 1973.
- (9) TRW Report 20634-6002-RU-00, "Evaluation of Digital Correction Techniques for ERTS Images," Interim Report for the period March 1973 - August 1973, September 1973.